

## FULL PAPER

# Heliocentric Distance Dependence of Zodiacal Light Observed by Hayabusa2#

Kohji Tsumura<sup>1\*</sup>, Shuji Matsuura<sup>2</sup>, Kei Sano<sup>3</sup>, Takahiro Iwata<sup>4,5</sup>, Hajime Yano<sup>4,5</sup>, Kohei Kitazato<sup>6</sup>, Kohji Takimoto<sup>3</sup>, Manabu Yamada<sup>7</sup>, Tomokatsu Morota<sup>8</sup>, Toru Kouyama<sup>9</sup>, Masahiko Hayakawa<sup>4</sup>, Yasuhiro Yokota<sup>4</sup>, Eri Tatsumi<sup>10</sup>, Moe Matsuoka<sup>11</sup>, Naoya Sakatani<sup>4</sup>, Rie Honda<sup>12</sup>, Shingo Kameda<sup>13</sup>, Hidehiko Suzuki<sup>14</sup>, Yuichiro Cho<sup>8</sup>, Kazuo Yoshioka<sup>15</sup>, Kazunori Ogawa<sup>16</sup>, Kei Shirai<sup>17</sup>, Hiroataka Sawada<sup>4</sup> and Seiji Sugita<sup>8,7</sup>

## Abstract

Zodiacal light (ZL) is sunlight scattered by interplanetary dust particles (IDPs) at optical wavelengths. The spatial distribution of IDPs in the Solar System may hold an important key to understanding the evolution of the Solar System and material transportation within it. The number density of IDPs can be expressed as  $n(r) \sim r^{-\alpha}$ , and the exponent  $\alpha \sim 1.3$  was obtained by previous observations from interplanetary space by Helios 1/2 and Pioneer 10/11 in the 1970s and 1980s. However, no direct measurements of  $\alpha$  based on ZL observations from interplanetary space outside Earth's orbit have been performed since then. Here, we introduce initial results for the radial profile of the ZL at optical wavelengths observed over the range 0.76-1.06 au by ONC-T aboard the Hayabusa2# mission in 2021-2022. The ZL brightness we obtained is well reproduced by a model brightness, although there is a small excess of the observed ZL brightness over the model brightness at around 0.9 au. The radial power-law index we obtained is  $\alpha = 1.30 \pm 0.08$ , which is consistent with previous results based on ZL observations. The dominant source of uncertainty arises from the uncertainty in estimating the diffuse Galactic light (DGL).

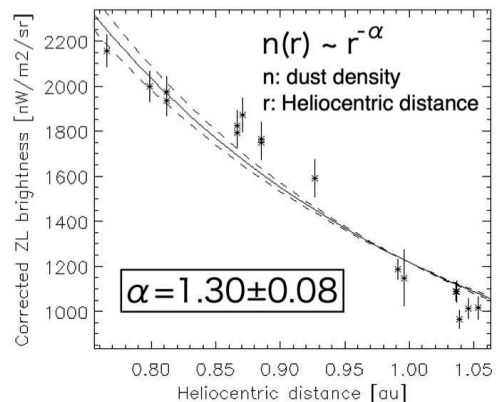
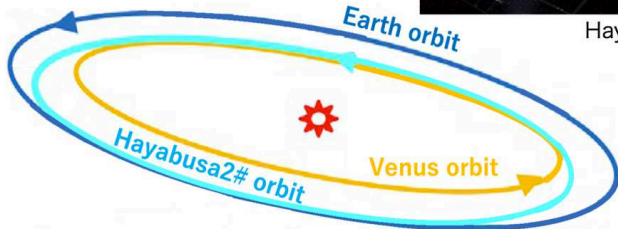
**Keywords:** zodiacal light; interplanetary dust; Hayabusa2#

## Graphical Abstract

Zodiacal light observation  
at 0.7 - 1 au by Hayabusa2#



Hayabusa2#



\*Correspondence: ktsumura@tcu.ac.jp

<sup>1</sup>Department of Natural Sciences, Faculty of Science and Engineering,  
Tokyo City University, 158-8557 Tokyo, Japan

Full list of author information is available at the end of the article

## 1 Introduction

The zodiacal light (ZL) is sunlight scattered by interplanetary dust particles (IDPs) at optical wavelengths, and it is a major constituent of the diffuse celestial brightness. A continuous supply of IDPs is necessary to sustain the diffuse brightness because IDP is removed from the Solar System due to the Poynting-Robertson (PR) effect and by radiation pressure from the Sun [1, 2]. Possible sources for this supply are asteroid collisions [3, 4, 5] or cometary ejections [6, 7, 8], but the relative ratios of the contributions from these sources are still unknown. Dust of interstellar origin also contributes  $\sim 10\%$  to the total amount of IDP [9]. Thus, observational constraints that can tell the differences among these sources are important for a better understanding the origin and characteristics of IDPs and of the way planetary and exoplanetary systems evolve with time [10, 11].

Historically, extensive ZL observations were conducted from ground-based telescopes at high-altitude sites in the 1960s and 1970s [12, 13], but the accuracy of these ZL observations is limited due to atmospheric emission. In contrast, space-based platforms eliminate atmospheric contamination and provide precise ZL measurements [14, 15, 16, 5, 17, 18, 19, 20, 21]. The ZL is the only sky-brightness component that is not fixed on the celestial sphere. In general, the ZL is smoothly distributed, and its small-scale spatial structures are only at the level of a few percent owing to the smooth spatial distribution of IDP as a smooth cloud [22]. The plane of symmetry of the smooth cloud is slightly inclined to the ecliptic plane because of the Jovian orbit. Seasonal variations in ZL occur for an Earth-based observer due to the orbital motion of the Earth, which changes the heliocentric distance and the position of the observer with respect to the symmetry plane. A detailed IDP distribution model has been established based on the seasonal variation of the ZL [23, 24].

The number density ( $n$ ) of IDP is presumed to be of a form that is separable into radial and vertical terms;

$$n(r, \beta) = n_0 \left( \frac{r}{r_0} \right)^{-\alpha} f(\beta), \quad (1)$$

where  $n_0$  is the reference number density of IDPs in the symmetry plane at the heliocentric distance  $r_0$ , and  $f(\beta)$  denotes the vertical distribution as a function of an elevation angle  $\beta$  from the symmetry plane [25]. The assumption that the vertical distribution of the IDPs depends only on  $\beta$  is suggested by the fact that the PR effect does not affect the orbital inclinations of particles as they spiral into the Sun. The radial power-law is induced by the radial distribution

expected for particles under the influence of the PR effect, which results in  $\alpha = 1$  for dust bound in a circular orbit [2]. When dust-grain sizes are reduced by sublimation near the Sun, such smaller dust particles are expelled from the Solar System as  $\beta$ -meteoroids by radiation pressure [26, 27, 28]. The radial profile of  $\beta$ -meteoroids is expected to follow a power law with  $\alpha = 2$  [29]. The relative ratio of these two components remains an open issue and may hold an important key for understanding the evolution of the IDP distribution [30, 31].

The ZL brightness  $I_{ZL}$  can be modeled as the integral of scattered sunlight along the line of sight:

$$I_{ZL} = \int F_{\odot}(r)n(r)A\Phi(\theta)dl, \quad (2)$$

where  $F_{\odot}(r) \sim r^{-2}$  is the Solar flux at the distance  $r$  from the Sun,  $A$  is the albedo of the IDP,  $\Phi(\theta)$  is the phase function at the scattering angle  $\theta$ , and  $dl$  is an increment along the line of sight. If the scattering properties (size and albedo) of IDPs do not change significantly with heliocentric distance, the heliocentric dependence of ZL toward the antisolar direction on the symmetry plane can be written as  $I_{ZL} \sim r^{-(\alpha+1)}$ . If the line of sight is not oriented in the antisolar direction, the heliocentric dependence of  $I_{ZL}$  becomes much more complex, since it depends on the phase function  $\Phi(\theta)$  for which  $\theta$  will vary. In addition, a heliocentric dependence of the local albedo of the IDPs has also been reported [32], which makes the heliocentric dependence of  $I_{ZL}$  even more complex.

Direct observations of the radial power-law index  $\alpha$  based on ZL observations were performed from spacecraft outside Earth's orbit in the 1970s and 1980s. Pioneer 10/11 observations of the ZL at 1-3.3 au gave  $\alpha = 1-1.5$ . More specifically, a single power-law model with  $\alpha \sim 1$  and a cutoff near 3.3 au gives the best fit to the observational data, although a two-component model with  $\alpha \sim 1.5$  and increased IDP in the asteroid belt fits the data equally well [33]. Helios 1/2 observations of the ZL at 0.3-1 au gave  $\alpha = 1.3 \pm 0.05$ , although  $\alpha = 1.35$  gives a better fit for small solar elongations ( $< 50^\circ$ ), and  $\alpha = 1.25$  is more appropriate for large solar elongations ( $> 100^\circ$ ) [34, 35]. ZL observations from spacecraft outside Earth's orbit have not been performed following these missions. The Japanese Venus orbiter Akatsuki tried but could not detect the ZL due to insufficient cooling of the sensor [36].

Some IDP distribution models were developed based on observations of the all-sky ZL brightness and its seasonal variation from geocentric orbit. In particular, observations from the Cosmic Background Explorer (COBE) yielded  $\alpha = 1.34 \pm 0.022$  [23] and  $\alpha = 1.22$

[24], and observations by AKARI gave  $\alpha = 1.59 \pm 0.02$  [37]. These observations of the ZL were performed at 1 au, so the accuracy in determining  $\alpha$  was worse than that obtained by direct observations from interplanetary space.

The value of  $\alpha$  has also been determined based on the observations of the inner ZL or F-corona. Observations of the inner ZL by Clementine from lunar orbit while the Sun was in eclipse behind the Moon yielded  $\alpha = 1.45 \pm 0.05$  [38]. Values of  $\alpha$  from 1.31 to 1.35 were obtained from F-corona observations at elongations ranging from 0.07 to 0.45 au from the Sun [39] by the Heliospheric Imager-1 [40] onboard the Solar TERrestrial RELations Observatory-A (STEREO-A) orbiting the Sun at approximately 1 au. In addition,  $\alpha = 1.31$  was obtained by F-corona observations between 0.1 and 0.4 au [41] by the Widefield Imager for Solar Probe inner telescope (WISPER-1) [42] onboard the Parker Solar Probe (PSP) when it passed perihelion at 0.16-0.25 au. These results are limited to dust distributions close to the Sun.

A technique for studying the distribution and properties of IDPs independent of the ZL observation is in-situ dust counting using dedicated dust detectors. The size distribution of IDPs was studied by the in-situ dust-counting method and it was suggested that large (10-100  $\mu\text{m}$ ) dust is dominant around 1 au [43, 44]. The ZL brightness is indicative of the IDP distribution in the inner Solar System, where the IDP density is substantial, and the IDP distribution derived from these ZL observations is confined to the inner Solar System ( $< 5$  au). Conversely, dust distribution in the outer Solar System has been investigated by the in-situ dust-counting method [45, 46].

This paper introduces the IDP distribution based on the ZL observations from the Hayabusa2# mission at 0.76-1.06 au performed in 2021-2022. These are the first successful observations of the ZL from outside Earth's orbit in the last 40 years.

## 2 Data Acquisition and Reduction

### 2.1 Hayabusa2# overview

Hayabusa2 is the second Japanese asteroid-sample-return mission. The Hayabusa2 spacecraft was launched in December 2014 and successfully arrived at asteroid (162173) Ryugu in June 2018. After extensive scientific observations for  $\sim 1.5$  years, it departed from Ryugu in November 2019 and successfully brought the capsule containing Ryugu samples back to Earth in December 2020 [50, 51]. With the successful main mission of the sample return completed, an extended mission named Hayabusa2# (SHARP; Small Hazardous Asteroid Reconnaissance Probe) was initiated to explore new asteroids; it will perform a fly-by of (98943) 2001

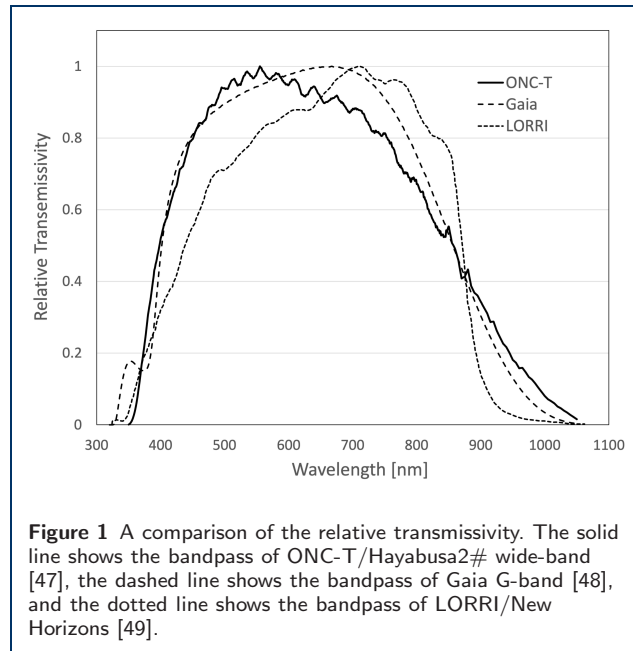


**Figure 1** A comparison of the relative transmissivity. The solid line shows the bandpass of ONC-T/Hayabusa2# wide-band [47], the dashed line shows the bandpass of Gaia G-band [48], and the dotted line shows the bandpass of LORRI/New Horizons [49].

CC21 in July 2026 and a rendezvous with 1998 KY26 in July 2031 [52]. Some scientific observations including ZL observations will be performed during this long cruising phase [53].

The Optical Navigation Camera (ONC) onboard Hayabusa2 consists of one telescopic camera (ONC-T) and two wide-angle view cameras (ONC-W1/W2) [54, 55, 47, 56, 57], and it was used for both global and local high-resolution optical observations of Ryugu [58]. The ONC was carefully calibrated both before and after launch, and it remains in good condition after contact with the surface of Ryugu during the two touchdowns for sampling. In this study, we used ONC-T for the ZL observations. The field of view of ONC-T is  $6.27 \times 6.27 \text{ deg}^2$ , which is covered with a  $1024 \times 1024$  pixel region of a CCD detector [54]. The longest exposure time of ONC-T was 178 sec, which we used for the ZL observations in this study. ONC-T has a wheel system that rotates seven color-bandpass filters and one wide clear filter (a panchromatic glass window). We used the wide-band filter ( $\lambda = 612 \text{ nm}$  and  $\Delta\lambda = 448 \text{ nm}$ , see Figure 1) for the ZL observations, with a v-band filter ( $\lambda = 550 \text{ nm}$  and  $\Delta\lambda = 28 \text{ nm}$ ) for stray light subtraction (see Section 2.5).

### 2.2 Observation Fields

The Hayabusa2 spacecraft followed an elliptical orbit over the range 0.76-1.06 au before the Earth swing-by on December 2027, as shown in Figure 2 and 3 [52]. The spacecraft maintained an attitude in which the solar-array paddle (+Z direction) was pointed toward the Sun during this period, and we performed the ZL

**Table 1** Spacecraft positions and observed fields

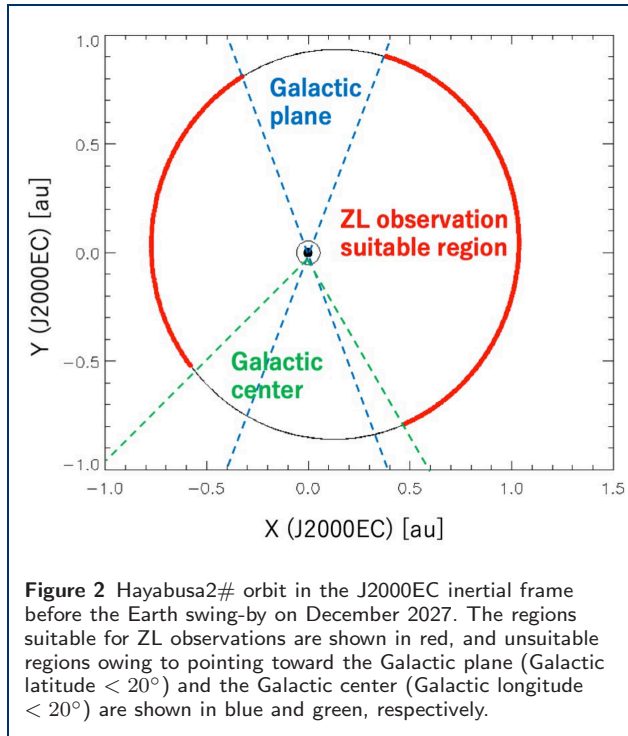
Date	Position of Spacecraft [au]				Observed Field [deg]			Solar Elongation
	X	Y	Z	R <sup>(1)</sup>	(RA, Dec)	(Elon, Elat) <sup>(2)</sup>	(Glon, Glat) <sup>(3)</sup>	
2021-08-23	1.023	0.252	-0.069	1.053	( 15.93, -3.65)	( 13.25, -9.64)	(130.58, -66.34)	174.10
2021-09-20	0.821	0.633	-0.047	1.037	( 37.06, 5.46)	( 36.52, -8.71)	(162.23, -49.88)	173.81
2021-11-29	-0.261	0.846	0.035	0.886	(104.42, 18.72)	(103.67, -4.03)	(196.79, 9.75)	172.78
2021-12-06	-0.375	0.781	0.042	0.866	(112.96, 18.16)	(111.80, -3.56)	(200.79, 16.88)	172.57
2021-12-28	-0.664	0.468	0.057	0.812	(142.74, 12.54)	(141.02, -2.05)	(219.94, 41.00)	172.84
2022-01-24 <sup>(4)</sup>	-0.774	-0.067	0.055	0.777	(198.38, 3.56)	(195.57, 10.49)	(316.49, 65.85)	167.64
2022-02-14 <sup>(4)</sup>	-0.625	-0.474	0.037	0.784	(204.83, -14.26)	(208.19, -3.68)	(320.08, 47.01)	169.01
2022-04-18	0.451	-0.810	-0.048	0.927	(297.25, -31.48)	(293.38, -10.22)	( 8.92, -25.26)	170.79
2022-05-16	0.834	-0.535	-0.071	0.991	(327.89, -25.02)	(321.52, -11.33)	( 25.45, -49.77)	170.76
2022-06-20	1.039	-0.024	-0.076	1.039	(357.99, -13.31)	(352.80, -11.40)	( 74.84, -70.40)	170.74
2022-07-04	1.028	0.193	-0.071	1.046	( 8.76, -8.29)	( 4.74, -11.08)	(110.55, -70.76)	170.74
2022-08-01	0.854	0.587	-0.051	1.036	( 30.13, 1.62)	( 28.62, -10.00)	(155.74, -56.78)	170.76
2022-08-29	0.505	0.858	-0.021	0.996	( 53.46, 10.57)	( 53.73, -8.38)	(174.72, -35.49)	170.80
2022-10-17	-0.318	0.811	0.038	0.871	(106.56, 17.81)	(105.80, -4.72)	(198.51, 11.20)	170.88
2022-11-14	-0.683	0.415	0.057	0.799	(144.53, 10.87)	(143.23, -3.08)	(222.98, 41.84)	170.95
2022-12-12	-0.750	-0.154	0.052	0.766	(184.25, -5.34)	(186.02, -3.21)	(287.28, 56.48)	171.00

(1)  $R = \sqrt{X^2 + Y^2}$ .

(2) Ecliptic coordinate.

(3) Galactic coordinate.

(4) These data were excluded from the analysis owing to the presence of additional stray light (see Section 2.5).



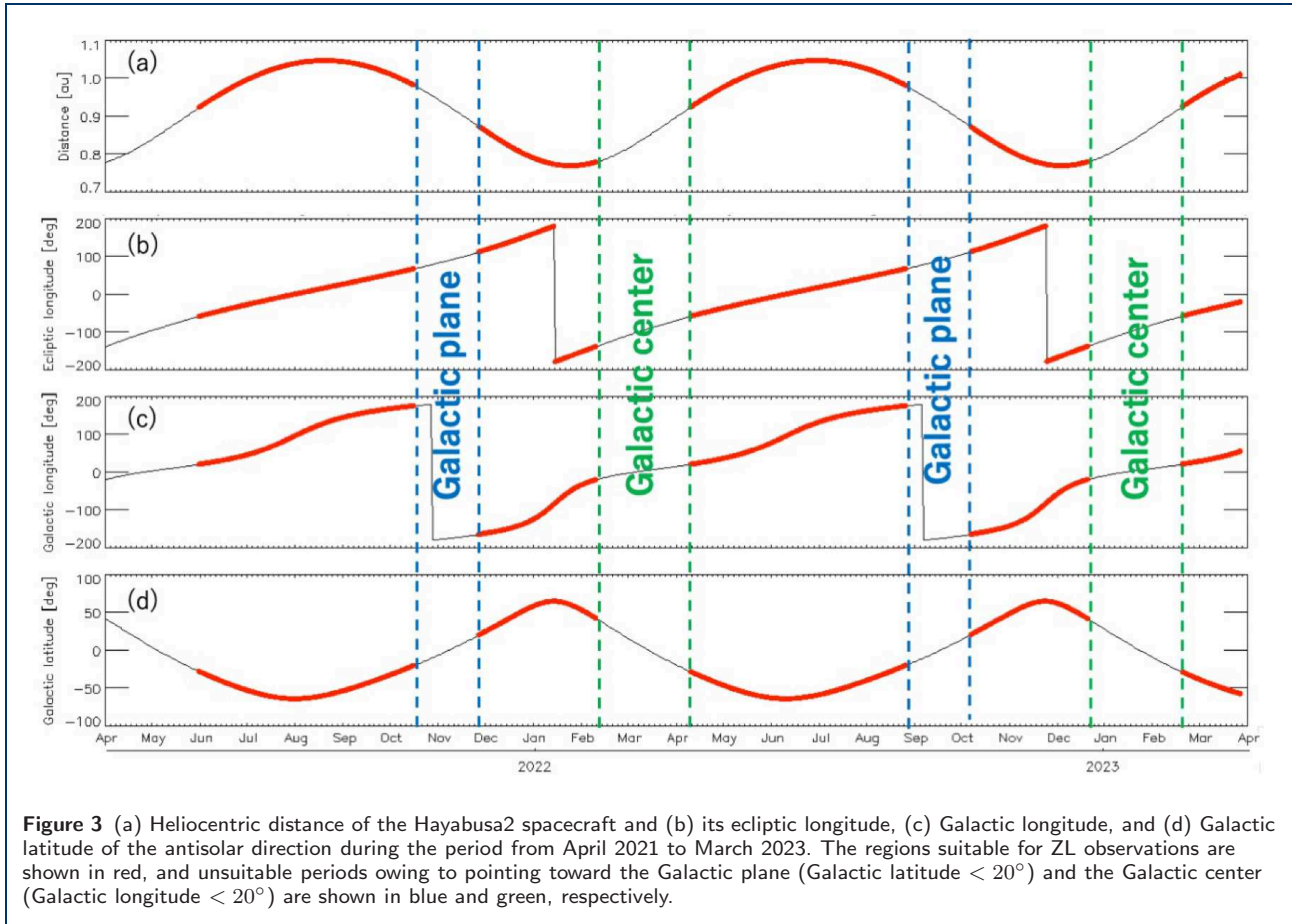
observations during periods when the ion engines were not in operation. Since ONC-T points toward the  $-Z$  direction, the ZL is observed toward the antisolar direction. This is an advantage of our ZL observations

over past observations because previous ZL observations in interplanetary space were made at various solar elongation angles, making it difficult to distinguish whether the ZL changes were due to changes in the heliocentric distance or in the solar elongation. In our ZL observations, the change in ZL brightness due to the solar elongation was minimized by observing the ZL at a nearly constant solar elongation (see Table 1).

Stray light is produced when sunlight hits the radiator that cools the ONC-T detector from a certain range of directions [55, 47]. Thus, the ZL observations need to be conducted in a “stray-light-avoidance attitude”, in which the  $-X$  side and  $+Y$  side of the spacecraft are illuminated by the Sun. For this reason, the actual directions of our ZL observations are shifted from the antisolar direction by  $\sim 10$  degrees. Table 1 summarizes the observed fields and the position of the spacecraft when the observations were conducted.

Periods when the observable direction (antisolar direction) is pointed toward either the Galactic plane or the Galactic center are not suitable for ZL observations because the Galactic brightness is too strong (see Section 3.1 and 3.2). Thus, we define as unsuitable ZL observation periods those in which the antisolar direction is pointing toward (1) Galactic latitude  $< 20^\circ$  (the blue zones in Figures 2 and 3) or (2) Galactic longitude  $< 20^\circ$  (the green zones in Figures 2 and 3). The ZL observations were made approximately once



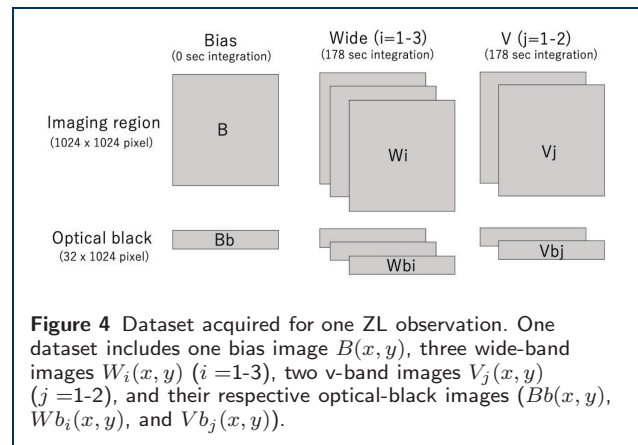


a month during the time suitable for ZL observations (the red zones in Figures 2 and 3).

### 2.3 Acquired Images

The ONC-T detector has a  $1024 \times 1024$  pixel imaging region, with a  $16 \times 1024$  pixel masked regions termed “optical black” on each side as a dark reference [54]. The two optical-black images are combined and treated as one  $32 \times 1024$  pixel optical-black image. Raw images acquired by ONC-T are processed in a sequence of steps to calibrate the image data. In this work, we used L2a-level images, which are raw FITS images with header information containing the spacecraft system housekeeping data and ONC status data (the temperatures of the detector, lens system, and electronics as well as the voltages of the electronics, etc.) [47]. The signal from each pixel is provided in 16-bit digital numbers (DN).

One ZL observation dataset includes one bias image  $B(x, y)$ , three wide-band images  $W_i(x, y)$  ( $i = 1-3$ ), two v-band images  $V_j(x, y)$  ( $j = 1-2$ ), and their respective optical-black images ( $Bb(x, y)$ ,  $Wb_i(x, y)$ , and  $Vb_j(x, y)$ ), as shown in Figure 4. For the ZL observations on 2021-11-29, 2021-12-06, 2021-12-28, 2022-01-



24, and 2022-02-14, as part of the calibration operations we acquired two data sets to monitor the stability of the ONC-T sensitivity after it was turned on.

### 2.4 Dark-Current Subtraction

Dark-current subtraction is essential for the measurement of diffuse radiation such as the ZL. We estimated the dark current for each image in our dataset from

the corresponding dark image, which we obtained from the optical-black image by subtracting a bias image ( $Wb_i(x, y) - Bb(x, y)$  and  $Vb_j(x, y) - Bb(x, y)$ ). We then created a histogram of the dark image, and we take its peak position to be the value of the dark current for that image. We fitted the histogram of the dark image with a Gaussian function. The peak position of the histogram corresponds to the mode of the dark image. Using this Gaussian-fitting procedure, we eliminated bad pixels such as those due to leakage of light from the imaging region or due to hot pixels caused by cosmic-ray hits. We expressed the resulting dark-current values for the wide-band and v-band images as  $I_{\text{dark}}^{W_i}$  and  $I_{\text{dark}}^{V_j}$ , respectively. As an example, we found the dark current of the first bias-subtracted optical-black image taken on 2022-08-29 to be  $I_{\text{dark}}^{W_1} = 5.92$  DN from the peak position of the histogram, as shown in Figure 5.

Next, the obtained dark current and the bias image are subtracted from the imaging region, yielding three wide-band subtracted images and two v-band subtracted images in one data set. From the wide-band images, we generated a single reduced image  $W(x, y)$  from three subtracted images by taking the median of each pixel:

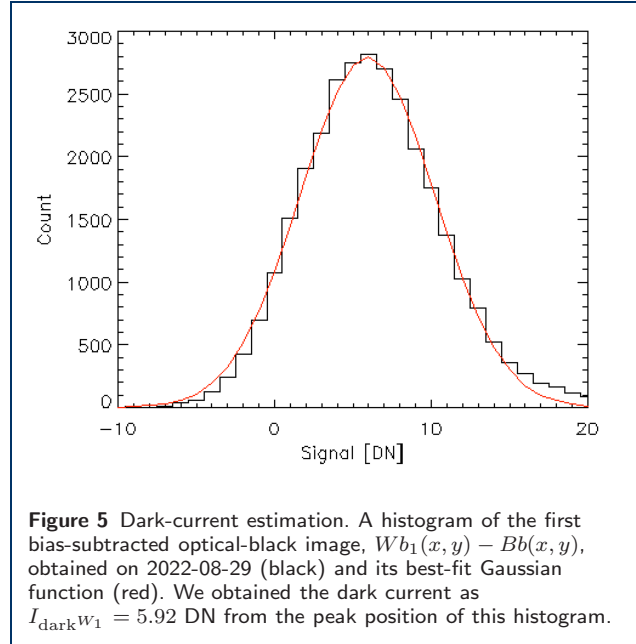
$$W(x, y) = \text{median}[W_i(x, y) - (B(x, y) + I_{\text{dark}}^{W_i})]. \quad (3)$$

This median procedure removes many hot pixels caused by cosmic-ray hits. Since there are only two v-band images, we cannot use the median procedure for them. Instead, we generated a single reduced image  $V(x, y)$  by taking the minimum of each pixel to reduce hot pixels caused by cosmic-ray hits:

$$V(x, y) = \min[V_j(x, y) - (B(x, y) + I_{\text{dark}}^{V_j})]. \quad (4)$$

## 2.5 Stray-Light subtraction

Since stray light occurs in ONC-T images when the spacecraft is at certain attitudes [55, 47], we performed all ZL observations in stray-light-avoidance attitudes (Section 2.2). However, weak stray light remains even in this case. Figures 6a and 6b the reduced wide-band image  $W(x, y)$  and v-band image  $V(x, y)$  obtained on 2021-08-23, respectively, and the stray-light patterns can be seen clearly in these images. It is known that the intensity and pattern of the stray light do not depend on the filter selection [55]. Thus, we subtracted the v-band image  $V(x, y)$  as a stray-light reference frame from the wide-band image  $W(x, y)$  to remove the remaining stray light, as shown in Figures 6c and 6d. Since the ZL signal in the v-band image is estimated

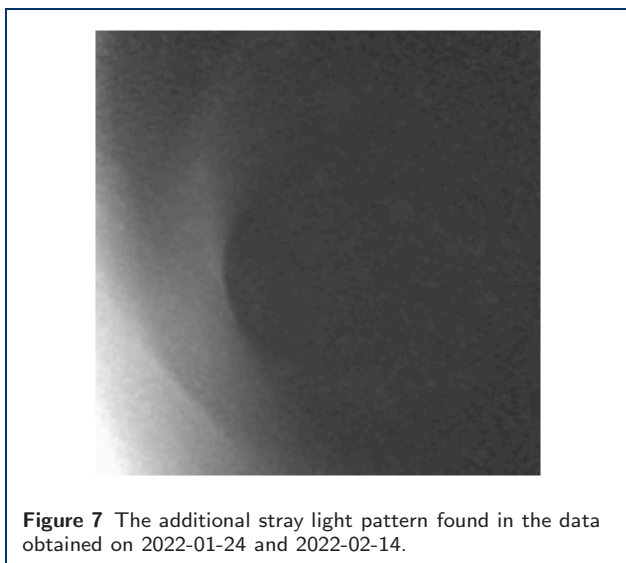
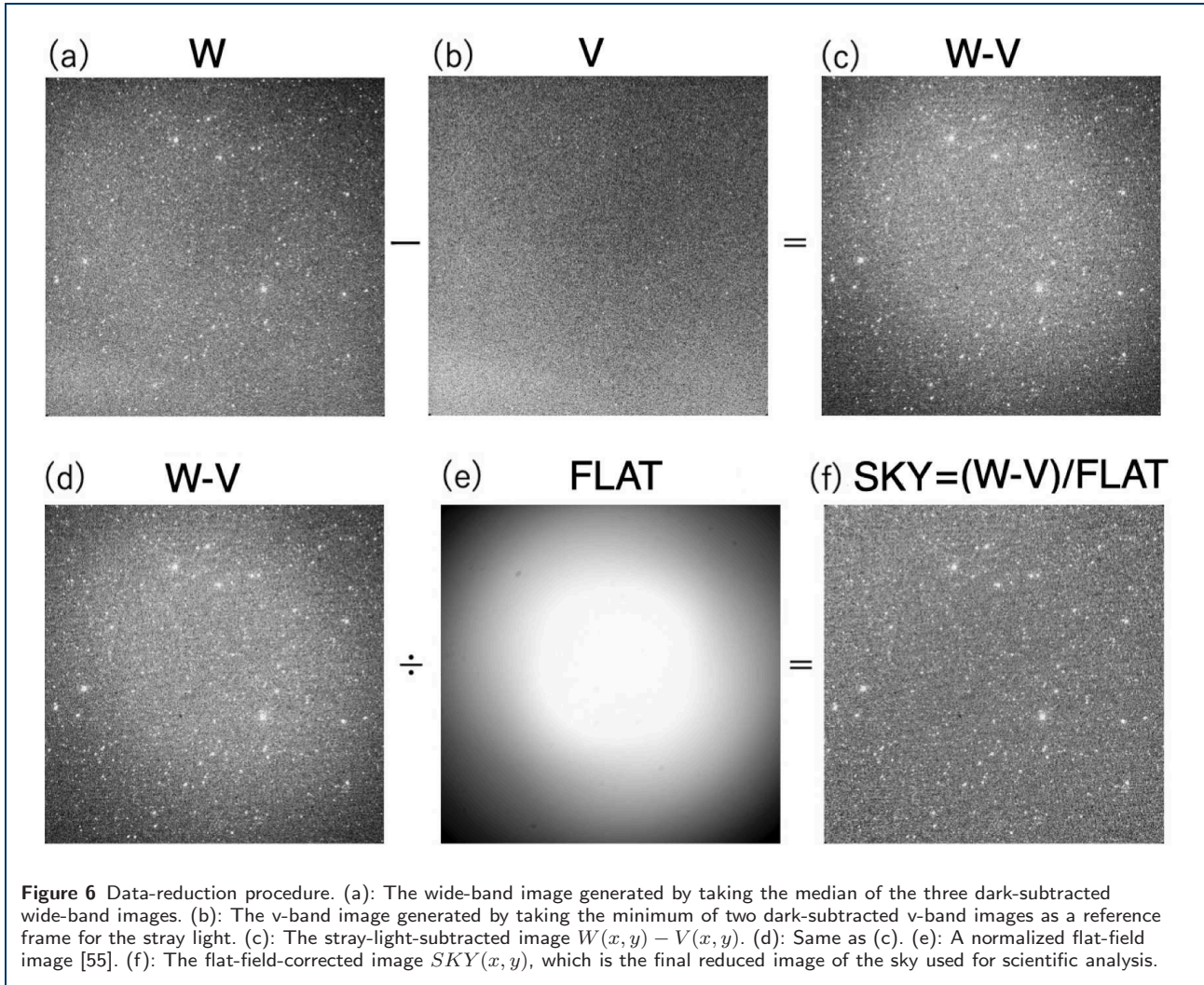


to be less than 1 DN, there is little impact on the scientific analysis of the ZL due to this stray-light-removal procedure.

We found an additional stray-light pattern in the data obtained on 2022-01-24 and 2022-02-14, as shown in Figure 7. Because this stray light appears only in the wide-band image, it cannot be removed by the v-band subtraction procedure. The source of this additional stray light is thought to be light scattered at the inner wall of the entrance hole of the ONC-T hood, as is indicated by the shape of the stray light (circular pattern). For this reason, we excluded data from these two days from subsequent analyses.

## 2.6 Flat-Field Correction

The stray-light-subtracted image  $W(x, y) - V(x, y)$  clearly shows a limb-darkening pattern (Figures 6c and 6d), which is the same pattern as in the flat-field image (Figure 6e) [47, 59]. This fact means that the detector is uniformly illuminated from the front of the optics, showing that the sky brightness has certainly been detected by the ONC-T. We corrected this limb-darkening pattern by dividing the image by the normalized flat-field image  $FLAT(x, y)$ , as shown in Figure 6f. Since we have not created a wide-band flat-field image, we used the v-band flat-field image instead. The wavelength dependence of the flat-field image is negligible because the detector is identical for both bands. The image obtained after the flat-field correction  $SKY(x, y)$  is the final reduced image of the sky



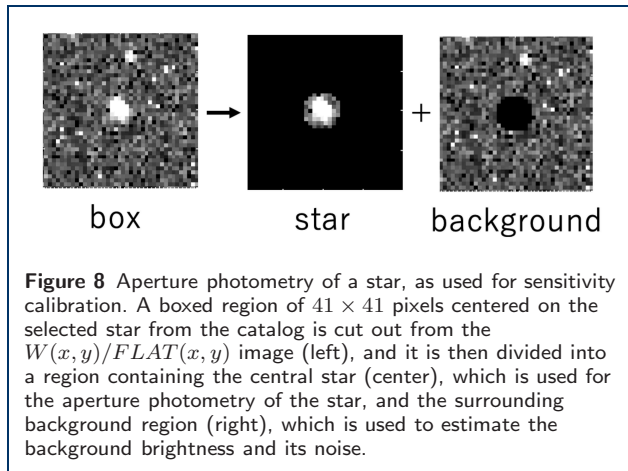
used for scientific analysis:

$$SKY(x, y) = \frac{W(x, y) - V(x, y)}{FLAT(x, y)}. \quad (5)$$

### 2.7 Sensitivity Calibration Using Stars

Degradation of the ONC-T sensitivity was reported after the two touchdown operations on the asteroid Ryugu [56, 57]. Consequently, we monitored and calibrated the sensitivity of the ONC-T in our data using the field stars in our images. For this sensitivity calibration, we used the  $W(x, y)/FLAT(x, y)$  image and not the  $SKY(x, y)$  image. This is because the flux for the bright stars used in this calibration process in case of the  $SKY(x, y)$  image is unsuitable for the sensitivity calibration as the v-band signal of the bright stars has been subtracted in the  $SKY(x, y)$  image. Although the  $W(x, y)/FLAT(x, y)$  image includes the stray light described in Section 2.5, it can be removed





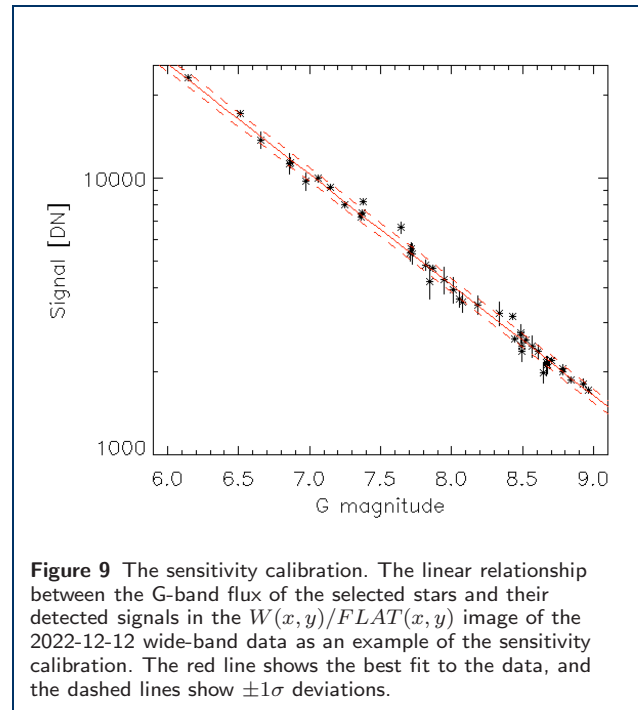
by the aperture-photometry procedure described below.

The sensitivity-calibration procedure for the wide-band is as follows. First, we solved the astrometry of the images from the distribution of the stars using the astrometry-calculation code Astrometry.net [60]. Next, we matched the bright stars in the image with those in the Gaia Data Release 3 (DR3) catalog [61, 62]. This catalog is suitable for our dataset because the wavelength coverage of Gaia's G-band, which is an unfiltered, white-light photometric band, is similar to that of our wide-band filter on ONC-T (Figure 1). The Gaia DR3 catalog contains around  $1.806 \times 10^9$  sources, with a limiting magnitude of about  $G \sim 21$  mag, with uncertainties of  $\sim 0.3$  mmag for  $G < 13$  mag, 1 mmag at  $G = 17$  mag, and 6 mmag at  $G = 20$  mag. We selected stars that meet the following criteria:

- The selected stars are in regions with stray-light intensities less than 20 DN in the  $V(x,y)$  image,
- The selected stars are in the region with normalized flat-field values greater than 0.8, and
- The selected stars have fluxes between the 6th and 9th AB magnitude in the G-band in the Gaia DR3 catalog.

Criteria (a) and (b) reduce the uncertainty caused by the reduction processes of stray-light subtraction and flat-field correction. The fraction of the area satisfying both criteria (a) and (b) is approximately 44% of the total detector area in the central region of the detector. Criterion (c) reduces the uncertainty in the photometry by selecting stars that have sufficient signal but are not saturated. The ONC-T detector is known to be linear up to  $\sim 3000$  DN, with  $< 1\%$  deviation [47], and the signal value of even the brightest pixel in an image of a 6th-magnitude star is approximately within this range.

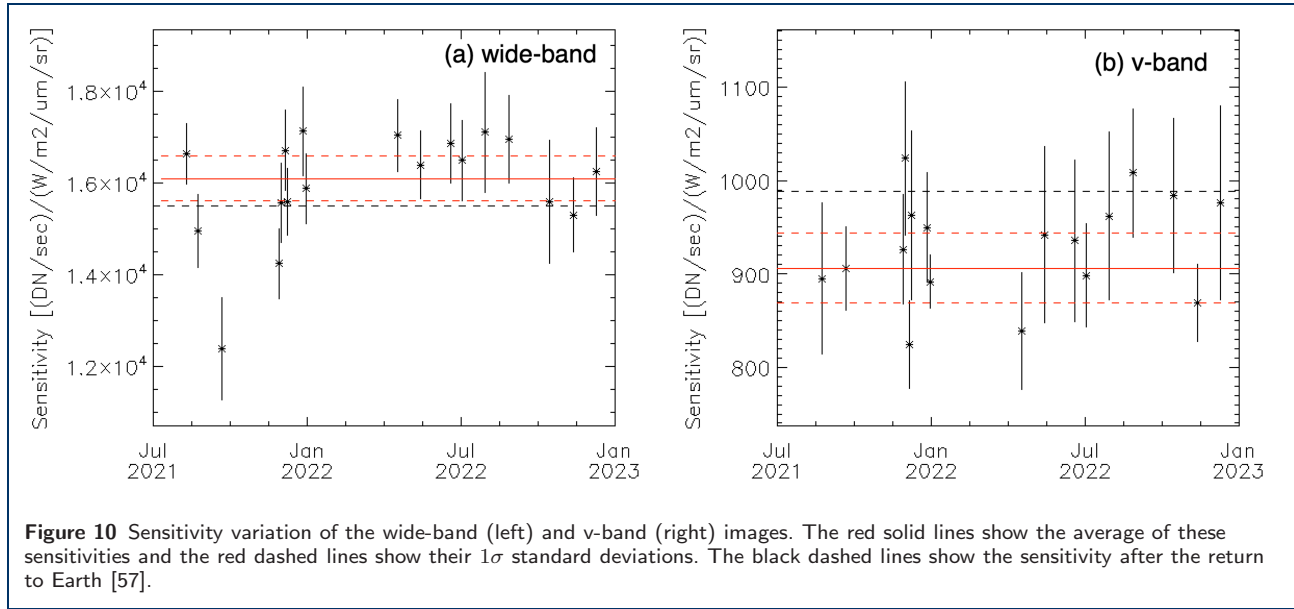
For aperture photometry, a boxed region of  $41 \times 41$  pixels centered on the selected star is cut out, and



this boxed region is divided into a region centered on the star and the surrounding background region, as shown in Figure 8. The radius of the circle used to cut out the star at the center is adjusted according to the G-band brightness of this star in the catalog. Next, all pixels greater than 20 DN are masked, as they are considered to be other astronomical objects (stars and galaxies) or hot pixels caused by cosmic-ray hits. We applied additional masks using a  $\sigma$ -clipping procedure to remove the remaining bright pixels. Then we examined all the masked images by eye and masked any additional remaining bad pixels. Subsequently, we calculated the background brightness and its noise by computing the average and standard deviation of the masked background region, and we subtracted the background brightness from the star region. We then calculated the flux from the central star by calculating the sum of the masked and background-subtracted star region and estimated its uncertainty based on the background noise. Figure 9 shows the relation between the G-band fluxes of the selected stars from the catalog and their detected signal in the 2022-12-12 data. A good linear relation between them exists in all the observed data, and we obtained the sensitivity in units of  $(\text{DN}/\text{sec})/(\text{W}/\text{m}^2/\mu\text{m}/\text{sr})$  by taking their ratio.

Figure 10 (left) shows the sensitivity calculated from our observed data as a function of time. The sensitivity obtained after the return to the Earth [57] is also shown. This figure shows that the degradation of the sensitivity has stopped and that the sensitivity has remained almost constant since the return to





the Earth. The average and standard deviation of the sensitivity after the  $\sigma$ -clipping procedure is  $16095 \pm 490$  (DN/sec)/(W/m<sup>2</sup>/μm/sr) (red solid and dashed lines, respectively, in Figure 10 left), which we applied to all the data to obtain the sky brightness of the wide-band images. We treated the standard deviation of the sensitivity as a systematic uncertainty (see Section 4.3).

We applied the same sensitivity-calibration procedure to the v-band data ( $V(x, y)/FLAT(x, y)$  images) to check the consistency of the result because the wide-band data and v-band data share the same detector. Gaia does not have a V-band filter, but it does have a blue band (BP) and a red band (RP), and the V-band magnitude can be estimated from the BP and RP magnitudes [48]. In the selection of stars for the v-band calibration, conditions (a) and (b) are the same as for the wide-band calibration, and condition (c) selects stars brighter than 8th mag in the converted V-band. Figure 10 (right) shows the sensitivity profile of the v-band, and we confirmed that the sensitivity remained constant in our dataset. The sensitivity and its  $1\sigma$  uncertainty we obtained for the v-band are  $906 \pm 37$  (DN/sec)/(W/m<sup>2</sup>/μm/sr).

## 2.8 Point-Spread Function

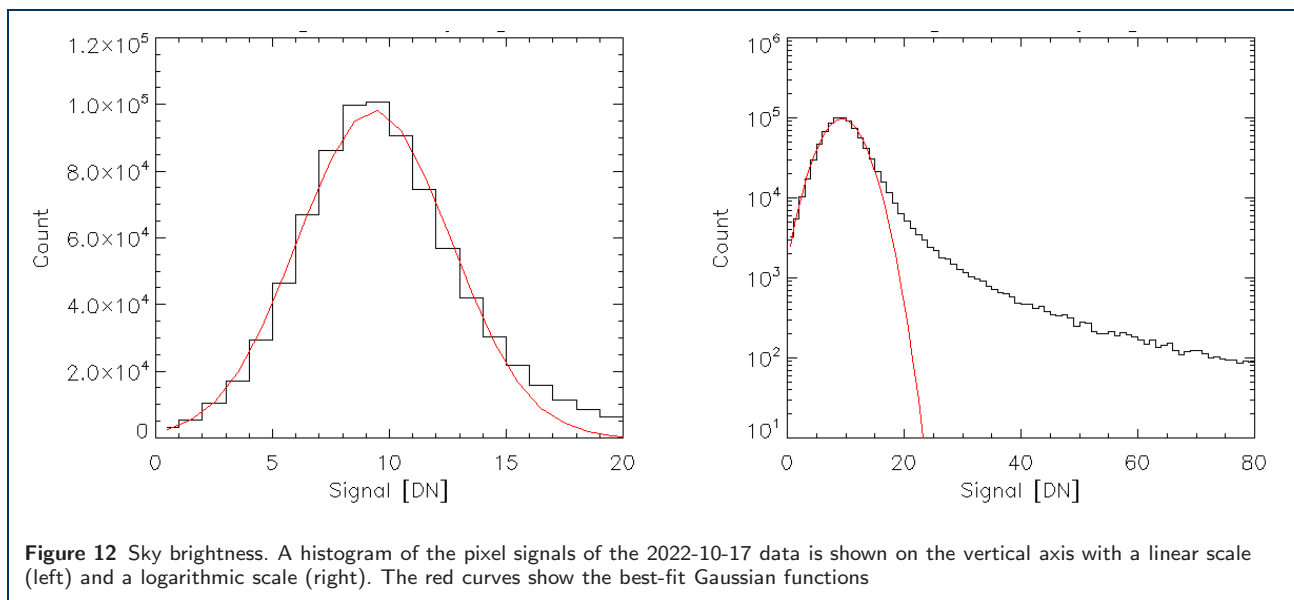
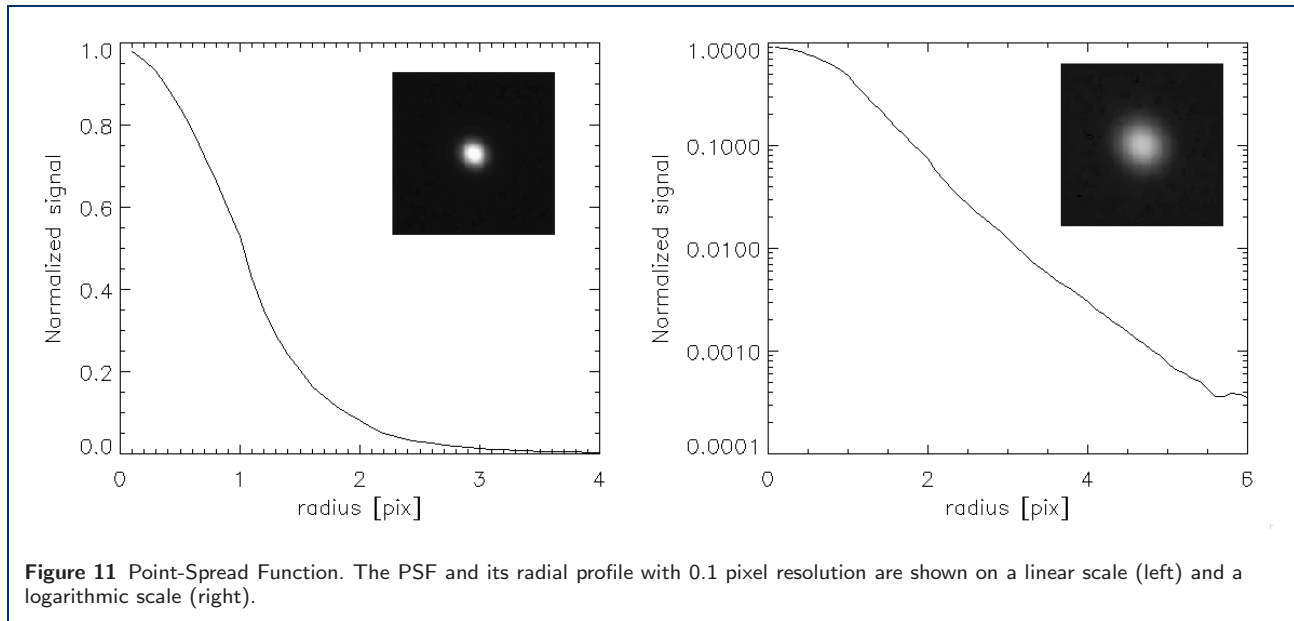
We obtained a template for the point-spread function (PSF) of the ONC-T wide-band image by adding the images of several bright stars. First, as suitable images for making the PSF template, we selected 56 objects with G-band magnitudes between 6th mag and 8th mag that have clean stellar images, with few bad pixels or without other objects around them. Then, we aligned these images with 0.1 pixel resolution and

added them together to obtain the PSF template. Figure 11 shows the resulting PSF template and its radial profile with 0.1 pixel resolution. The full-width half maximum (FWHM) of the PSF is 2.00 pixels, which is consistent with previous measurements [56].

## 2.9 Sky Brightness

We obtained the sky brightness as the signal value of dark pixels with no stars nor hot pixels by cosmic-ray hits in the  $SKY(x, y)$  image, using the histogram method employed to determine the dark current described in Section 2.4. We created a histogram of the  $SKY(x, y)$  image, including stars and hot pixels, and obtained the best-fit Gaussian curve. Figure 12 shows the histogram of the  $SKY(x, y)$  image and its best-fit Gaussian curve for the 2022-10-17 data. Since the  $SKY(x, y)$  image is dominated by dark pixels with no stars nor hot pixels, the peak of the pixel histogram of the  $SKY(x, y)$  image represents the sky brightness. We separate the higher signal tail of bright stars and the dark sky signals in the pixel histogram by the Gaussian fitting as shown in Figure 12, and we treated the  $1\sigma$  error in the peak position as the statistical uncertainty in the sky brightness. We converted the resulting sky brightness from DN units to  $\lambda I_\lambda$  in nW/m<sup>2</sup>/sr units by applying the calibration factor obtained in Section 2.7. Using this procedure, the systematic uncertainty in the calibration factor is transferred to a systematic uncertainty in the sky brightness. Table 2 summarizes the obtained sky brightness and its statistical and systematic uncertainties.

At this point, the detection limit has not been determined (this is obtained in the next subsection using



the sky brightness and its standard deviation). As it is not known how faint stars should be masked based on the star catalog, we determined the sky brightness by creating a histogram of the entire  $SKY(x, y)$  image without masking the stars. This method worked well because the number of pixels observing dark sky is much larger than the number observing stars and other astronomical objects. Note that the stars detected in the images are masked when we determine the ZL as described in Section 3.4.

### 2.10 Limiting Magnitude

It is important to know the limiting magnitude in our observed images because we need to mask the detected stars to derive the diffuse brightness of the sky. As shown in Figure 12, the histogram of the  $SKY(x, y)$  image has a side lobe caused by the detected stars in the images, which exceeds the best-fit Gaussian curve. The width ( $\sigma$ ) of the Gaussian corresponds to the standard deviation of the fluctuation in the sky brightness, and we define the limiting magnitude as the brightness of stars for which three pixels in the center of the PSF (Figure 11) exceed  $+2\sigma$  of the sky deviation. We set the uncertainty in determining the limiting magni-

**Table 2** Obtained sky brightness and backgrounds with their uncertainties.

Date	SKY <sup>(1)</sup>	ISL <sup>(1)</sup>	DGL <sup>(1)</sup>	ZL <sup>(1)</sup>	Corr. factor <sup>(2)</sup>	limmag <sup>(3)</sup>
2021-08-23	961.1 ± 23.2 ± 29.3	28.1 ± 2.2	34.2 ± 2.6 ± 27.6	889.3 ± 16.1 ± 40.3	1.142	12.79 ± 0.18
2021-09-20	1047.8 ± 6.0 ± 31.9	34.2 ± 2.7	33.2 ± 2.5 ± 25.9	958.4 ± 8.8 ± 41.1	1.135	12.80 ± 0.19
2021-11-29 <sup>(4)</sup>	1922.1 ± 12.1 ± 58.6	299.4 ± 15.1	46.9 ± 3.3 ± 30.3	1602.5 ± 17.4 ± 65.9	1.091	12.63 ± 0.16
2021-11-29 <sup>(4)</sup>	1937.1 ± 10.8 ± 59.0	299.1 ± 15.1	46.9 ± 3.3 ± 30.3	1619.5 ± 17.3 ± 66.3	1.091	12.63 ± 0.16
2021-12-06 <sup>(4)</sup>	1864.2 ± 9.8 ± 56.8	156.1 ± 8.4	32.5 ± 2.3 ± 22.1	1670.6 ± 11.3 ± 61.0	1.092	12.70 ± 0.17
2021-12-06 <sup>(4)</sup>	1819.9 ± 9.4 ± 55.4	155.8 ± 8.6	32.5 ± 2.3 ± 22.1	1642.8 ± 11.7 ± 59.7	1.091	12.70 ± 0.17
2021-12-28 <sup>(4)</sup>	1882.5 ± 10.1 ± 57.4	45.0 ± 3.1	24.4 ± 1.8 ± 18.6	1809.2 ± 7.9 ± 60.3	1.092	12.72 ± 0.17
2021-12-28 <sup>(4)</sup>	1885.6 ± 10.0 ± 57.4	45.7 ± 3.1	24.4 ± 1.8 ± 18.6	1770.7 ± 8.2 ± 60.4	1.092	12.71 ± 0.17
2022-04-18	1599.7 ± 11.0 ± 48.7	186.3 ± 8.3	68.7 ± 5.0 ± 49.1	1358.8 ± 12.3 ± 69.2	1.172	12.69 ± 0.17
2022-05-16	1052.9 ± 18.9 ± 32.1	57.0 ± 3.8	16.7 ± 1.3 ± 13.0	988.3 ± 9.3 ± 34.6	1.202	12.76 ± 0.18
2022-06-20	857.3 ± 32.7 ± 26.1	31.8 ± 2.4	15.1 ± 1.2 ± 12.2	806.1 ± 13.9 ± 28.8	1.198	12.74 ± 0.18
2022-07-04	928.0 ± 9.4 ± 28.3	27.9 ± 2.1	25.7 ± 2.0 ± 20.9	850.2 ± 8.0 ± 35.2	1.190	12.77 ± 0.18
2022-08-01	994.2 ± 15.2 ± 30.3	31.7 ± 2.4	17.2 ± 1.3 ± 13.7	927.5 ± 8.2 ± 33.2	1.172	12.79 ± 0.18
2022-08-29	1196.4 ± 12.8 ± 36.4	38.7 ± 2.7	132.9 ± 9.9 ± 99.2	1002.4 ± 14.2 ± 105.7	1.147	12.79 ± 0.18
2022-10-17	1984.2 ± 9.4 ± 60.4	251.7 ± 12.4	45.2 ± 3.2 ± 29.6	1698.3 ± 14.6 ± 67.3	1.102	12.62 ± 0.16
2022-11-14	1854.4 ± 9.3 ± 56.5	44.5 ± 2.9	20.0 ± 1.5 ± 15.2	1792.9 ± 7.6 ± 58.5	1.114	12.69 ± 0.17
2022-12-12	1997.9 ± 7.8 ± 60.9	37.0 ± 2.6	23.6 ± 1.8 ± 18.8	1923.5 ± 6.8 ± 63.7	1.121	12.70 ± 0.17

(1) Brightness in  $\lambda I_\lambda$  and its statistical and systematic uncertainty in  $\text{nW}/\text{m}^2/\text{sr}$ .

(2) Correction factor used to obtain the ZL brightness toward the antisolar direction in the ecliptic plane (see Section 4.2).

(3) Limiting magnitude in the G-band (see Section 2.10).

(4) Two data sets were acquired on the same day (see Section 2.3).

tude to be 1 DN, which is equivalent to approximately 0.2 mag uncertainty in the limiting magnitude. The limiting magnitude of each image and its uncertainty are summarized in Table 2.

Stars brighter than the limiting magnitude were extracted from the Gaia DR3 catalog (see Section 2.7), convolved with the PSF (see Section 2.8), and distributed in the image to create a Gaia bright-star image, as shown in Figure 13 (b). The distribution of stars in this Gaia bright-star image reproduces well the distribution of the stars detected in the image observed by ONC-T (Figure 13 (a)), indicating the validity of the detection limits determined by the method described above. We used the Gaia bright-star image as a stellar mask to conceal stars when obtaining the ZL (see Section 3.4).

### 3 Background Subtraction

#### 3.1 Integrated Starlight

Stars fainter than the limiting magnitude are not detected as point sources in the observed images, but the sum of the light from those undetected stars, called integrated starlight (ISL), contributes to the sky brightness. Therefore, the ISL must be estimated and subtracted from the sky brightness to obtain the ZL.

The ISL image  $ISL(x, y)$  for each field is produced by stars fainter than the limiting magnitude extracted from the Gaia DR3 catalog, as shown in Figure 13 (c). The average brightness of each ISL image and its  $1\sigma$  statistical uncertainty are listed in Table 2. Since the

ISL at optical wavelengths saturates when the contributions from stars down to 20th mag are added [10], the depth of the Gaia DR3 catalog is sufficient. The photometric uncertainty in the catalog is negligible compared with the uncertainty of the limiting magnitude of ONC-T.

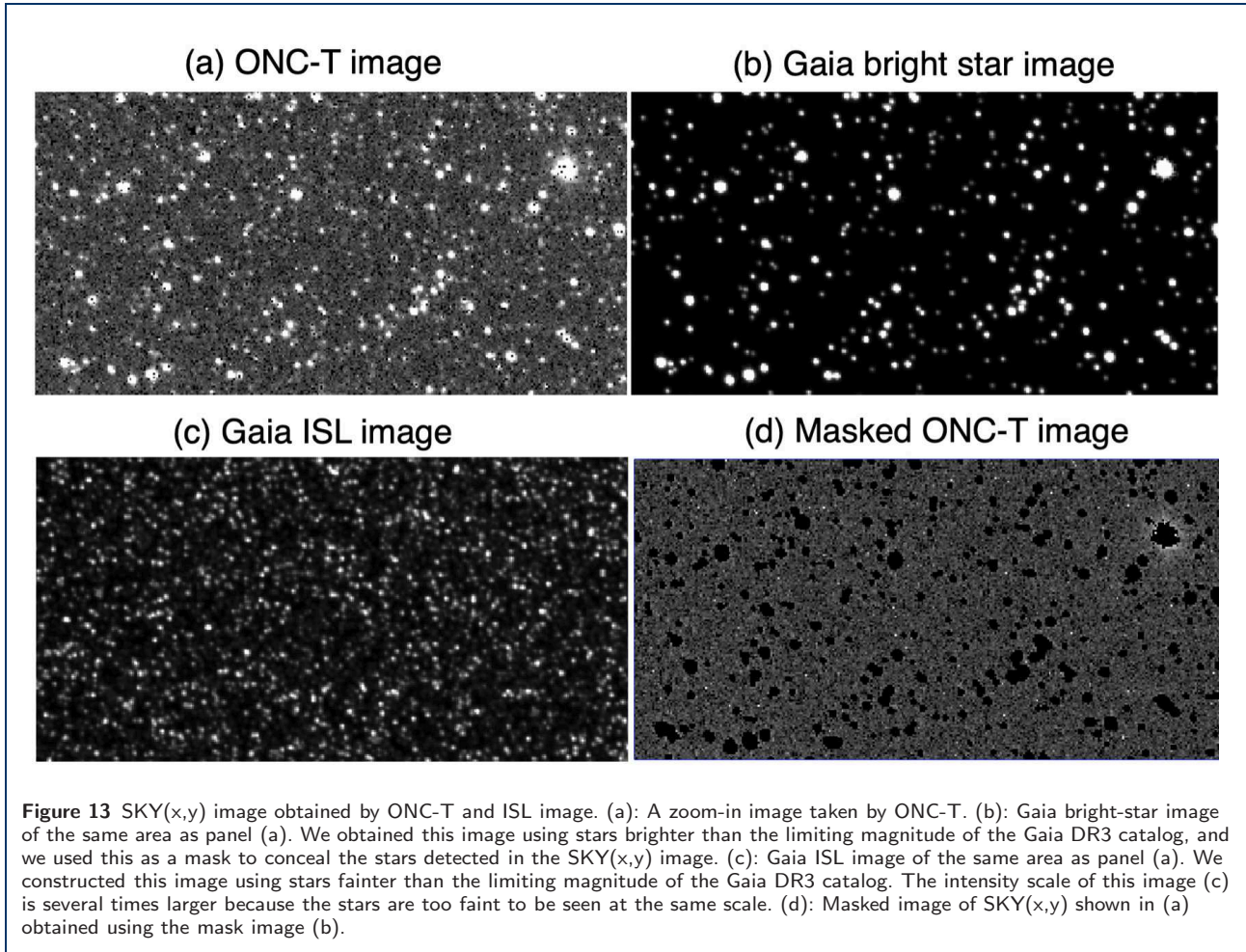
#### 3.2 Diffuse Galactic Light

Diffuse Galactic light (DGL) consists of starlight scattered by interstellar dust in our Galaxy [63], and it also must be subtracted from the sky brightness to obtain the ZL. A method commonly used to estimate the DGL is to use its correlation with the thermal emission from interstellar dust in the far infrared. The intensity map at  $\lambda = 100 \mu\text{m}$ , which is a reprocessed composite of the COBE and IRAS maps (SFD map [64]), is commonly used as a template for the interstellar dust distribution. Thus,

$$\lambda I_{DGL} = \nu\beta_\lambda \cdot d(Glat) \cdot I_{SFD}, \quad (6)$$

where  $\lambda I_{DGL}$  is the DGL brightness in  $\text{nW}/\text{m}^2/\text{sr}$ ,  $I_{SFD}$  is the far-infrared intensity at  $100 \mu\text{m}$  from the SFD map in  $\text{MJy}/\text{sr}$ ,  $d(Glat)$  is a geometric function of the Galactic latitude ( $Glat$ ), and  $\nu\beta_\lambda$  is the DGL correlation factor in  $(\text{nW}/\text{m}^2/\text{sr})/(\text{MJy}/\text{sr})$ . As discussed in [65], this geometric function is given by

$$d(Glat) = d_0(1 - 1.1g\sqrt{|\sin|Glat|}), \quad (7)$$



where  $d_0$  is a normalizing parameter, and  $g$  is the asymmetry factor of the scattering phase function [66].

This DGL correlation factor at optical and near-infrared wavelengths has been derived in many previous studies [67, 68, 69, 70, 71, 72, 73, 74, 75], but there are two different results. Recently, the values  $\nu\beta_\lambda = 3.54 \pm 0.91$  (nW/m<sup>2</sup>/sr)/(MJy/sr),  $d_0 = 1.76$ , and  $g = 0.61$  have been reported from results obtained by the Long-Range Reconnaissance Imager (LORRI) on New Horizons [75]. These results were obtained at 10-50 au from the Sun, where the ZL is negligible. The bandpass of LORRI is also similar to that of the wide-band filter of ONC-T (Figure 1). However, this DGL estimate is about 5-10 times smaller than many previous results. For example,  $\nu\beta_\lambda = 21.0 \pm 0.9$  [(nW/m<sup>2</sup>/sr)/(MJy/sr)] and  $d(\text{Glat}) = 1$  (the geometric function was not considered) at  $0.65 \mu\text{m}$  was found based on observations from the Hubble Space Telescope (HST) [73]. In the present work, we treat the DGL estimate based on the New Horizons result as a low-level DGL estimate, that based on the HST result as a high-level DGL estimate, and the average of these two DGL estimates as a

middle-level DGL estimate. We treat the difference between the low-level and the high-level DGL estimates as a systematic uncertainty.

The spatial resolution of the SFD map (6.1 arcmin) is insufficient relative to our data from ONC-T (22 arcsec). Therefore, we used a far-infrared, all-sky diffuse map based on the AKARI all-sky survey [76, 77] in this study. Because these AKARI all-sky diffuse maps cover wider wavelength ranges with finer spatial resolution and better signal-to-noise ratio than the SFD map, they can serve as a new template for the DGL estimate, replacing the SFD map. In this study, we used the AKARI Wide-S ( $\lambda = 90 \mu\text{m}$ ) map, for which the spatial resolution is  $\sim 1.3$  arcmin. One difference between these maps is that point sources have not been removed from the AKARI Wide-S map, whereas they have been removed from the SFD map. Therefore, we masked all the point sources included in the AKARI Far-Infrared Bright Source Catalogue Version 2 [78]. Figure 14 compares the SFD map (left) and AKARI Wide-S map (center) in the field of 2022-08-23, which



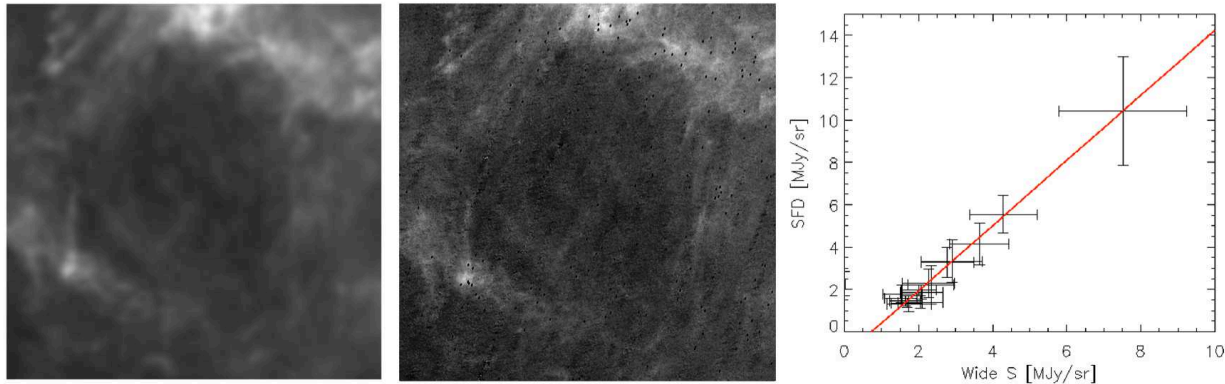


**Figure 14** Diffuse Galactic Light. Left: DGL image for the field of 2021-08-23 based on the SFD map at  $\lambda = 100 \mu\text{m}$  [64]. Center: DGL image for the same field based on the AKARI Wide-S map at  $\lambda = 90 \mu\text{m}$  [76, 77] after masking the point sources. Right: Comparison of the intensities from the SFD map and the AKARI Wide-S map of our observation fields. The red line shows the best fit to this correlation.

shows that the AKARI Wide-S map has better spatial resolution than the SFD map

The publicly available AKARI Wide-S map has a ZL remainder that must be subtracted because only the smooth cloud component of the ZL has been subtracted from the raw data, and other ZL components, such as asteroidal dust bands, have not been subtracted [76]. The contribution from the unsubtracted ZL components is recognizable in the Wide-S map in the low-ecliptic-latitude region that we study in this work. There is a good linear correlation between the SFD map and the AKARI Wide-S map [77], but the AKARI Wide-S map at low ecliptic latitudes shows deviations from the linear correlation owing to the residual ZL that remains to be subtracted. Therefore, we used the data that other ZL components are additionally subtracted from the public AKARI Wide-S map based on a ZL asteroidal-dust-band model [79]. We confirmed the good correlation between the SFD map and the additionally ZL-subtracted AKARI Wide-S map, as shown in Figure 14 (right). This correlation is fitted by the equation

$$I_{\text{SFD}} = a \times I_{\text{Wide-S}} + c \quad (8)$$

where  $I_{\text{Wide-S}}$  is the far-infrared intensity from the AKARI Wide-S map in MJy/sr, and  $a$  and  $c$  are the fitting parameters. We obtained  $a = 1.54 \pm 0.05$  and  $c = -1.20 \pm 0.14$  MJy/sr in our observation fields, which are consistent with the result based on the all-sky data [76, 77]. We converted the AKARI Wide-S maps in our observation fields into DGL images  $DGL(x, y)$  using equations (6) and (8).

Another issue in the AKARI Wide-S map is the sky coverage. The AKARI all-sky map has  $> 99\%$  coverage

of the whole sky, but our observation fields contain regions with missing data. We therefore used SFD data for the missing regions in the AKARI Wide-S map. The middle-level DGL brightness based on the AKARI Wide-S map and its statistical and systematic uncertainties are listed in Table 2.

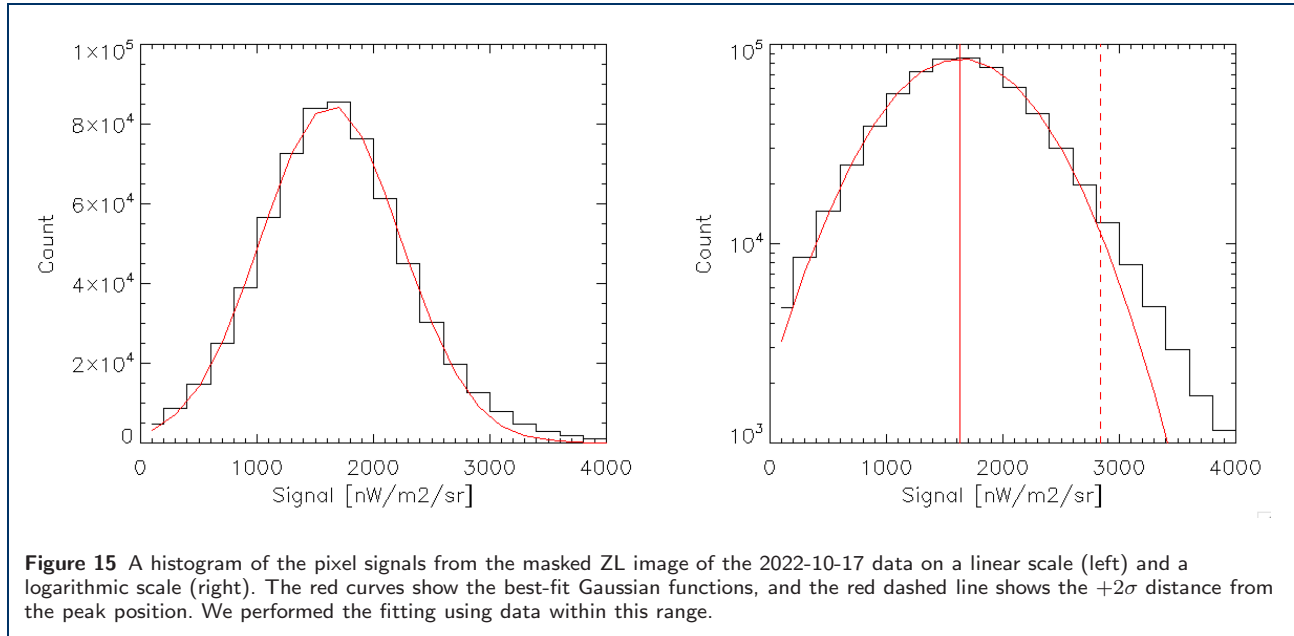
### 3.3 Extragalactic Background Light

Extragalactic background light (EBL) arises from emissions integrated from the first era of star production to the present day. Recent observations have shown that the EBL measured at optical and near-infrared wavelengths has an excess over the cumulative light from galaxies [80, 81, 82, 83, 84, 85, 86, 87, 75, 88, 89], which means that there are unknown light sources in the universe. The sources for this excess are still under discussion, but some candidates that have been proposed include intra-halo light [90, 91], primordial black holes formed by the collapse of the first halos [92], the decay of hypothetical particles [93], nearby black holes observed as faint compact objects [94, 95], and a warm-hot intergalactic medium [96]. We adopted  $\lambda I_{\text{EBL}} = 21.98 \pm 1.83$  nW/m<sup>2</sup>/sr at  $\lambda = 0.44\text{--}0.87 \mu\text{m}$ , as observed by LORRI/New Horizons [75]. We created an EBL image  $EBL(x, y)$  with all pixels having this value.

### 3.4 Zodiacal Light

The ZL is obtained by subtracting the background emissions from the observed sky brightness:

$$ZL(x, y) = SKY(x, y) - ISL(x, y) - DGL(x, y) - EBL(x, y). \quad (9)$$



We first subtracted the ISL image (Section 3.1), DGL image (Section 3.2), and EBL image (Section 3.3) from the SKY image (Section 2.6) to obtain the ZL image,  $ZL(x, y)$ , and we masked the stars detected in the ZL image (Section 2.10). As shown in Figure 13 (d), this masking procedure works well for almost all stars, although the peripheries of some of the brightest stars are not masked perfectly and are smeared out. We then created a histogram of the area where  $FLAT(x, y) > 0.5$  and stray light  $< 20$  DN (see Section 2.7) for each masked ZL image, and we regard its peak position and its  $1\sigma$  error estimate as the brightness and statistical uncertainty of the ZL (Figure 15). The systematic uncertainty in the ZL comes from the systematic uncertainties in the calibration and the DGL. Comparing the histograms of the masked ZL image (Figure 15) with the SKY image (Figure 12) shows that the excess of the side lobe over the Gaussian has been reduced thanks to the stellar masking. There is still a small excess owing to the smeared peripheries of the brightest stars and to some hot pixels caused by cosmic-ray hits, but this small excess has little effect on the peak position of the Gaussian because we performed the Gaussian fitting on data within a  $+2\sigma$  range from the peak (the red dashed line in Figure 15). The resulting estimate of the ZL and its uncertainties are listed in Table 2 and shown in Figure 16 (black).

## 4 Discussion

### 4.1 Absolute ZL brightness

We have compared the ZL brightness we observed with that predicted by the Kelsall model, which is based on

observations of the all-sky ZL brightness obtained from COBE observations at infrared wavelengths [23]. We calculated the ZL model brightness using the ZodiPy code [97], which implements the Kelsall model. The shortest wavelength for which the ZL brightness can be calculated with this model is  $1.25 \mu\text{m}$ , which is outside the range of the ONC-T wide-band data used in this study. However, the ZL at both  $1.25 \mu\text{m}$  and optical wavelengths (i.e., the ONC-T wide-band filter) results from scattered sunlight, and its spectral shape is the same irrespective of ecliptic latitude [5]. We therefore determined the ZL brightness at optical wavelengths by extrapolating from the model brightness at  $1.25 \mu\text{m}$  using the solar spectrum [98]. This extrapolation was performed using the ratio of the solar spectrum at  $0.612 \mu\text{m}$  and  $1.25 \mu\text{m}$ . Since the IDP reflectance varies by about 10% between  $1.25 \mu\text{m}$  and optical wavelengths [5, 84, 99], we have assumed a 10% uncertainty in the ZL model brightness at optical wavelengths associated with this extrapolation. Figure 16 compares the observed ZL brightness with the model brightness, which shows that they are consistent with each other within the ranges of uncertainties.

Gegenschein appears in the antisolar direction, and the Kelsall model does not include it. However, our observed fields are shifted from the antisolar direction by  $\sim 10$  degrees (see Table 1), and the Gegenschein is negligible there [100].

There are small excesses of the observed ZL brightness over the model brightness at around 0.9 au, as shown in Figure 16. This structure may be real, but we cannot confirm this at this point due to the paucity

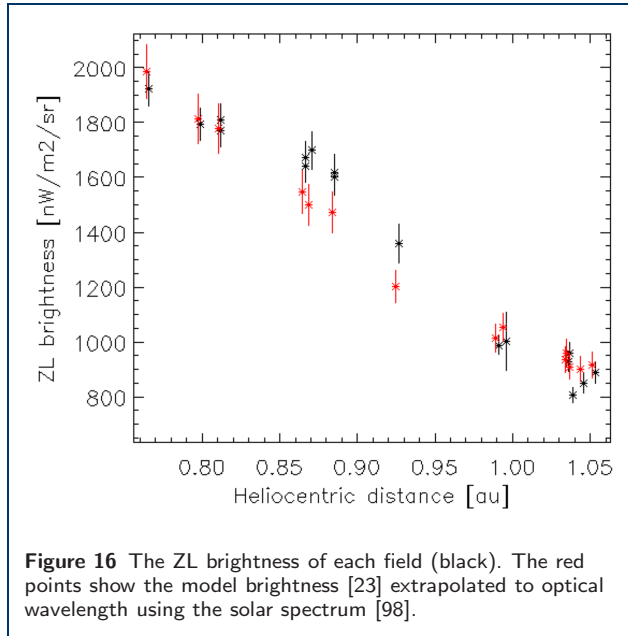


**Figure 16** The ZL brightness of each field (black). The red points show the model brightness [23] extrapolated to optical wavelength using the solar spectrum [98].

of data points. Verification will require the accumulation of data from future observations.

#### 4.2 Field-Variance Correction

Since the ZL brightness measurements were obtained at different ecliptic latitudes and solar elongations, a correction for the field variance is necessary to compare them under the same conditions in order to obtain the radial profile of the ZL. We performed this field-variance correction based on the Kelsall model. We calculated the seasonal average of the ZL model brightness toward the antisolar direction in the ecliptic plane at various heliocentric distances, as shown in Figure 17 (left, red). The radial power-law index of this calculated ZL model brightness is  $\alpha = 1.34$  because this value is used in the Kelsall model. We compared this ZL brightness toward the antisolar direction with the ZL model brightness toward the fields observed by ONC-T (Figure 17, left, black). We multiplied the observed ZL brightness by the ratio of these two ZL model brightnesses at each position as correction factors in order to obtain the ZL brightness toward the antisolar direction in the ecliptic plane (Figure 17 right). These correction factors are listed in Table 2.

Since this correction relies on the Kelsall model with  $\alpha = 1.34$ , it is not self-consistent if the obtained value of  $\alpha$  deviates significantly from 1.34. As we discuss in the next subsection, however, the value of  $\alpha$  we obtained from our observations is close to 1.34, so consequently this correction works. In addition, the field variance was corrected for local brightness difference at the same elongations but different ecliptic coordinates,

**Table 3** Obtained radial power-law index  $\alpha$  for each systematic uncertainty case.

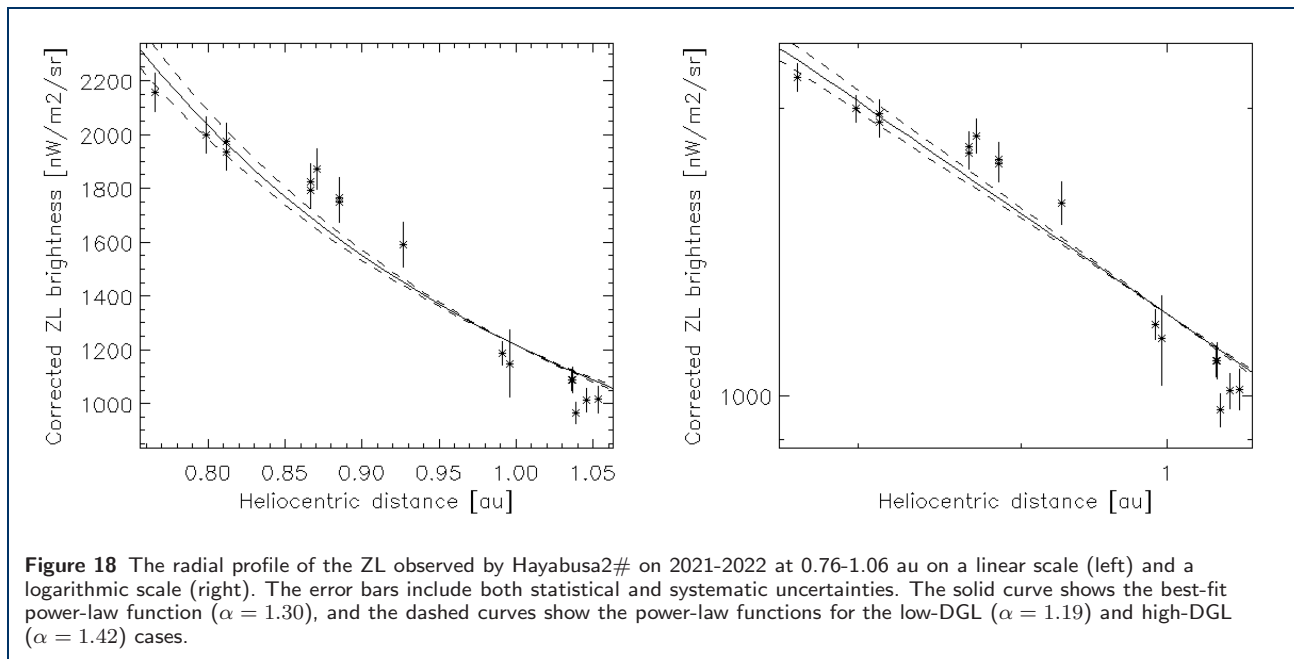
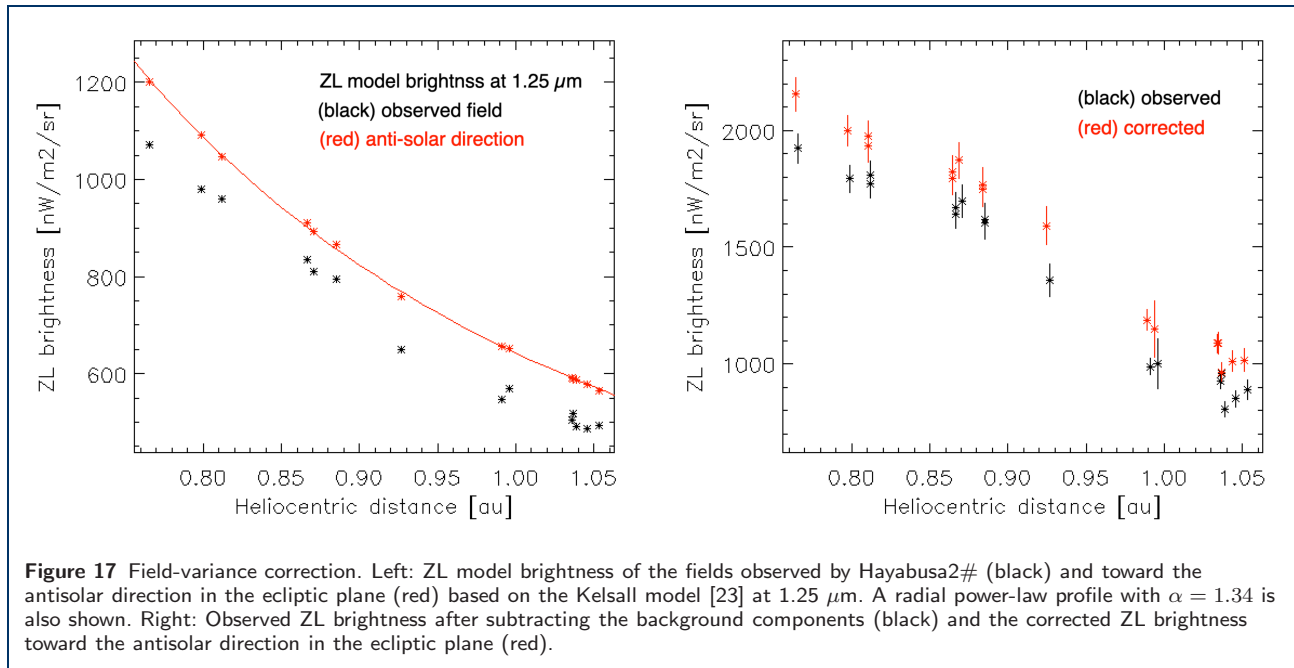
Calibration	DGL	Value of $\alpha$
low	low	$1.19 \pm 0.02$
nominal	low	$1.22 \pm 0.02$
high	low	$1.21 \pm 0.02$
low	middle	$1.29 \pm 0.02$
nominal	middle	$1.28 \pm 0.02$
high	middle	$1.31 \pm 0.02$
low	high	$1.38 \pm 0.02$
nominal	high	$1.37 \pm 0.02$
high	high	$1.42 \pm 0.02$

so the correction is not sensitive to  $\alpha$  which represents the global distribution of IPD.

#### 4.3 Dependence on Heliocentric Distance

Based on the corrected ZL brightness, we calculated the radial power-law index  $\alpha$  using the following method. The ZL brightness has two types of uncertainties: statistical uncertainties and systematic uncertainties. Statistical uncertainties appear randomly at each data point, while systematic uncertainties appear with a certain tendency at each data point. Our data contain two types of systematic uncertainties, one due to calibration (see Section 2.7) and the other due to DGL (see Section 3.2). We therefore calculated the radial power-law index  $\alpha$  for a total of  $3 \times 3$  cases (three cases for calibration uncertainty and three cases for DGL uncertainty). Table 3 shows the values of  $\alpha$  we obtained for each of these systematic-uncertainty cases. As this table shows, the calibration uncertainty does not have a significant impact on the value of  $\alpha$ , since the data points only go up and down overall. On the other hand, the DGL uncertainty does have a significant impact on the value of  $\alpha$ . From all of these values, we obtain  $\alpha = 1.30 \pm 0.08$  as the final result. Figure 18 shows the radial profile of the ZL and the best-fit power-law function. Again, the excess structure at  $\sim 0.9$  au can be seen in Figure 18.

Table 4 and Figure 19 compare the value of  $\alpha$  we obtained with previous results, and they show that our result is consistent with them. Since it is difficult to determine the radial profile of the IDP density from ZL observations obtained in a geocentric orbit or from F-corona observations, direct observations of the radial profile of the ZL from interplanetary space outside Earth's orbit are more reliable for this purpose. Our observations are the first successful observations of ZL from interplanetary space in the 40 years since Helios 1/2 and Pioneer 10/11. In addition, the ZL intensity varies with both the heliocentric distance and the solar elongation, both of which varied in the previous observations by Helios 1/2 and Pioneer 10/11.



On the other hand, we confined our observations to the antisolar direction (solar elongation  $\sim 180$  deg), so we can impose changes in ZL brightness on changes in heliocentric distance.

Values of  $\alpha$  greater than 1 are obtained from all the ZL observations, even though  $\alpha = 1$  is expected if the orbital evolution of the IDP is dominated by the PR effect [2]. This difference is caused by dust production due to the collision of dust particles [101, 43], dust supplied by comets around 1 au [102], the finiteness of the

dust cloud [103], or the heliocentric dependence of the local albedo of the IDP [104, 32]. In fact, a heliocentric dependence of the local albedo of the form  $r^{-0.3 \pm 0.1}$  has been reported [32], which partially explains  $\alpha$  being greater than 1.

The IDPs falling into the Sun due to the PR effect decrease in size owing to evaporation, and such small IDPs are blown away by radiation pressure as  $\beta$ -meteoroids. The radial profile of  $\beta$ -meteoroids is expected to follow a power law with  $\alpha = 2$ , and recent



**Table 4** Comparison of the radial power-law index  $\alpha$ .

Value of $\alpha$	Coverage of $\alpha$	Method	Observation wavelength	Observation site	Instrument	Reference
1 – 1.5	1 – 3.3 au	ZL observation	B, R bands	Interplanetary space	Pioneer 10/11	[33]
$1.3 \pm 0.05$	0.3 – 1 au	ZL observation	U, B, V bands	Interplanetary space	Helios 1/2	[34]
$1.34 \pm 0.022$	> 1 au	ZL observation	1.25–240 $\mu\text{m}$	Geocentric orbit	COBE	[23]
1.22	> 1 au	ZL observation	1.25–240 $\mu\text{m}$	Geocentric orbit	COBE	[24]
$1.45 \pm 0.05$	0.06 – 0.6 au	F-corona	0.5–0.9 $\mu\text{m}$	Lunar orbit	Clementine	[38]
$1.59 \pm 0.02$	> 1 au	ZL observation	9 $\mu\text{m}$ , 18 $\mu\text{m}$	Geocentric orbit	AKARI	[37]
$1.34^{(1)}$	1 – 3.3 au	ZL observation	B, R bands	Interplanetary space	Pioneer 10/11	[99]
1.31 – 1.35	0.07 – 0.45 au	F-corona	0.63–0.73 $\mu\text{m}$	Heliocentric orbit	STEREO-A	[39]
1.31	0.1 – 0.4 au	F-corona	0.49–0.74 $\mu\text{m}$	Interplanetary space	PSP	[41]
2	0.17 – 0.7 au	Dust counting	—	Interplanetary space	PSP	[29]
$1.30 \pm 0.08$	0.76 – 1.06 au	ZL observation	0.39–0.84 $\mu\text{m}$	Interplanetary space	Hayabusa2#	This work

(1) the Kelsall model is assumed.

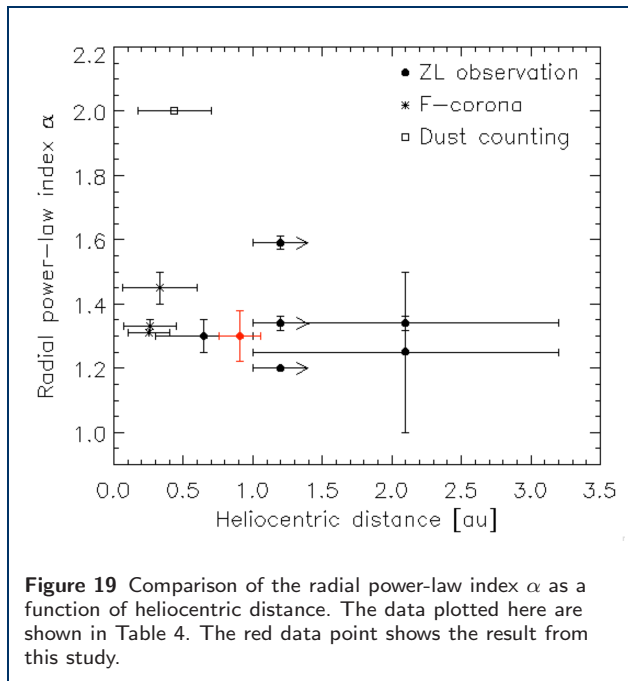


**Figure 19** Comparison of the radial power-law index  $\alpha$  as a function of heliocentric distance. The data plotted here are shown in Table 4. The red data point shows the result from this study.

in-situ direct counting of the flux of IDPs experienced by the PSP does show  $\alpha = 2$  in the range 0.17 – 0.7 au [29]. On the other hand, the reddening [5] and polarization [20, 21] of the ZL spectrum indicate that the majority of IDPs seen as ZL are large ( $> 1 \mu\text{m}$ ); smaller IDPs do not contribute much to the ZL even though they do exist [28]. While the value  $\alpha = 2$  obtained by the IDP impact-counting method is sensitive to small IDPs, the values of  $\alpha$  between 1 and 2 obtained from ZL observations are sensitive to larger IDPs. The small dust particles become hotter than the larger ones [105], and a hot component in the thermal emission from IDPs has been found using mid-infrared spectroscopy at  $\lambda = 3\text{--}6 \mu\text{m}$  [106, 107, 108, 17]. We would therefore expect to obtain the value  $\alpha \sim 2$  from ZL observations at  $\lambda = 3\text{--}6 \mu\text{m}$  carried out outside Earth's orbit be-

cause small dust particles with high temperatures are mainly observed in this wavelength range.

#### 4.4 Future Observations

Since ZL observations at 0.7–1 au by Hayabusa2# will continue until the Earth swing-by at the end of 2027, the accuracy of the results we have reported here will be improved through the accumulation of additional observational data. In particular, the excess structure at  $\sim 0.9$  au needs to be verified by accumulating data during this phase. After the second Earth swing-by in 2028, the Hayabusa2 spacecraft will fly to an orbit in the 1–1.5 au range [52], so we will be able to obtain the radial profile in the outer regions of the Solar System.

Before this orbital change of Hayabusa2#, we will have a chance to observe the radial profile of the ZL in the 1–1.5 au range from the Martian Moons eXploration (MMX) spacecraft, which is a Japanese sample-return mission from the Martian satellite Phobos [109]. The MMX is scheduled for launch in 2024 and arrival at Mars in 2025, and we are proposing to conduct simultaneous multi-wavelength (350–1000 nm) ZL observations during this cruising phase using the Optical Radiometer composed of Chromatic Imagers (OROCHI) onboard MMX [110].

In addition, we are developing an EXo-Zodiacal Infrared Telescope (EXZIT), with the aim of installing it on a spacecraft to Jupiter or farther [111, 112]. If this instrument can be realized, we will be able to observe the radial profile of the ZL at 1–5 au as well as the EBL without the ZL foreground above 3 au. We are also considering adding mid-infrared capabilities to EXZIT, which would allow us to examine our prediction of the  $\alpha \sim 2$  index for the ZL radial profile owing to small particles.

In-situ direct dust counting is also important for comprehending the IDP distribution in the Solar System because it provides independent estimates of the radial variation of the IDP density. More quantitative

comparisons between the ZL observations and in-situ direct dust counting are envisioned for future projects, which will provide us with the differences in the distributions according to dust size and parent bodies.

## 5 Summary

We observed the ZL brightness at optical wavelengths at 0.76–1.06 au with ONC-T on the Hayabusa2# mission. We detected a small excess of the observed ZL brightness over the model brightness at around 0.9 au, but we cannot determine whether or not this structure is real at this stage due to the paucity of data points. The radial power-law index we obtained is  $\alpha = 1.30 \pm 0.08$ , and the uncertainty in this estimate is dominated by the uncertainty due to the DGL estimate. This result is consistent with previous results based on other ZL observations.

### Acknowledgements

The Hayabusa2 spacecraft was developed and built under the leadership of the Japan Aerospace Exploration Agency (JAXA), with contributions from the German Aerospace Center (DLR) and the Centre National d'études Spatiales (CNES), and in collaboration with NASA, Nagoya Univ., The Univ. of Tokyo, National Astronomical Observatory of Japan (NAOJ), Univ. of Aizu, Kobe Univ., and other universities, institutes, and companies in Japan. This work has made use of the data obtained with AKARI, a JAXA project with the participation of the European Space Agency (ESA). This work also has made use of data from the ESA mission Gaia (<https://www.cosmos.esa.int/gaia>), processed by the Gaia Data Processing and Analysis Consortium (DPAC, <https://www.cosmos.esa.int/web/gaia/dpac/consortium>). Funding for the DPAC has been provided by national institutions, in particular, the institutions participating in the Gaia Multilateral Agreement. This research has made use of the VizieR catalog access tool, CDS, Strasbourg, France (DOI : 10.26093/cds/vizieR). The original description of the VizieR service was published in [113]. The authors thank Takafumi Ootsubo (NAOJ) for providing the ZL-subtracted AKARI Wide-S data, and Teresa Symons (University of California, Irvine) and Michael Zencov (Rochester Institute of Technology) for discussion on DGL estimate based on New Horizons.

### Funding

K. Tsumura was supported by JSPS KAKENHI Grant Number 20H04744 and Tokyo City University Prioritized Studies.

### Abbreviations

CNES: Centre National d'études Spatiales; COBE: Cosmic Background Explorer; DARTS: Data Archives and Transmission System; DGL: Diffuse Galactic light; DN: digital number; DPAC: Data Processing and Analysis Consortium; DR: Data release; EBL: Extragalactic background Light; ESA: European Space Agency; EXZIT: Exo-Zodiacal Infrared Telescope; FWHM: Full-width half maximum; HST: Hubble Space Telescope; IDP: Interplanetary dust particles; ISL: Integrated star light; JAXA: Japan Aerospace Exploration Agency; LORRI: Long-Range Reconnaissance Imager; MMX: Martian Moons eXploration; NAOJ: National Astronomical Observatory of Japan; ONC: Optical Navigation Camera; OROCHI: Optical RadiOmeter composed of CHromatic Imagers; PR effect: Poynting-Robertson effect; PSF: Point spread function; PSP: Parker Solar Probe; STEREO: Solar TERrestrial RELations Observatory; WISPER: Widefield Imager for Solar Probe inner telescope; ZL: Zodiacal light.

### Availability of data and materials

The raw datasets of this study will be made available in the Hayabusa2 Science Data Archives on the Data Archives and Transmission System (DARTS) repository, at <https://www.darts.isas.jaxa.jp/planet/project/hayabusa2/>. The analyzed datasets of this study are available from the corresponding author upon reasonable request.

### Competing interests

No competing interest is declared.

### Authors' contributions

K.Ts. analyzed the data and wrote the manuscript. S.M., K.Sa., T.I., and K.Ta. contributed to the data analysis. M.Y., T.M., T.K., M.H., Y.Y., E.T., M.M., N.S., R.H., S.K., H.Su., K.Y., Y.C., K.O., K.Sh., H.Sa., and S.S. contributed to ONC data acquisitions and reduction. M.Y. contributed to preparing the operation sequence for the ZL observations. All authors discussed the results and approved the final manuscript.

### Author details

<sup>1</sup>Department of Natural Sciences, Faculty of Science and Engineering, Tokyo City University, 158-8557 Tokyo, Japan. <sup>2</sup>Department of Physics, School of Science and Technology, Kwansai Gakuin University, 669-1337 Hyogo, Japan. <sup>3</sup>Department of Space Systems Engineering, School of Engineering, Kyushu Institute of Technology, 804-8550 Fukuoka, Japan. <sup>4</sup>Institute of Space and Astronautical Science, Japan Aerospace Exploration Agency, 252-5210 Kanagawa, Japan. <sup>5</sup>Department of Space and Astronautical Science, The Graduate University of Advanced Studies, 240-0193 Kanagawa, Japan. <sup>6</sup>Department of Computer Science and Engineering, The University of Aizu, 965-8580 Fukushima, Japan. <sup>7</sup>Planetary Exploration Research Center, Chiba Institute of Technology, 275-0016 Chiba, Japan. <sup>8</sup>Department of Earth and Planetary Science, University of Tokyo, 113-0033 Tokyo, Japan. <sup>9</sup>Digital Architecture Research Center, National Institute of Advanced Industrial Science and Technology, 135-0064 Tokyo, Japan. <sup>10</sup>Instituto de Astrofísica de Canarias, University of La Laguna, Tenerife, Spain. <sup>11</sup>Geological Survey of Japan, National Institute of Advanced Industrial Science and Technology, 305-8567 Ibaraki, Japan. <sup>12</sup>Center for Data Science, Ehime University, 790-8577 Ehime, Japan. <sup>13</sup>Rikkyo University, 171-8501 Tokyo, Japan. <sup>14</sup>Meiji University, 214-8571 Kanagawa, Japan. <sup>15</sup>Department of Complexity Science and Engineering, University of Tokyo, 277-8561 Chiba, Japan. <sup>16</sup>JAXA Space Exploration Center, Japan Aerospace Exploration Agency, 252-5210 Kanagawa, Japan. <sup>17</sup>Kobe University, 657-8501 Hyogo, Japan.

### References

- Wyatt SP, Whipple FL. The Poynting-Robertson effect on meteor orbits. *ApJ*. 1950 Jan;111:134–141.
- Burns JA, Lamy PL, Soter S. Radiation forces on small particles in the solar system. *Icarus*. 1979;40(1):1–48. Available from: <https://www.sciencedirect.com/science/article/pii/0019103579900502>.
- Dermott SF, Nicholson PD, Burns JA, Houck JR. Origin of the Solar System dust bands discovered by IRAS. *Nature*. 1984 Dec;312(5994):505–509. Available from: <https://doi.org/10.1038/312505a0>.
- Schramm LS, Brownlee DE, Wheelock MM. Major Element Composition of Stratospheric Micrometeorites. *Meteoritics*. 1989 Jun;24(2):99.
- Tsumura K, Battle J, Bock J, Cooray A, Hristov V, Keating B, et al. OBSERVATIONS OF THE NEAR-INFRARED SPECTRUM OF THE ZODIACAL LIGHT WITH CIBER. *ApJ*. 2010 Jul;719(1):394–402. Available from: <https://doi.org/10.1088/0004-637x/719/1/394>.
- Liou JC, Dermott SF, Xu YL. The contribution of cometary dust to the zodiacal cloud. *Planet Space Sci*. 1995;43(6):717–722. Available from: <https://www.sciencedirect.com/science/article/pii/003206339500065D>.
- Nesvorný D, Jenniskens P, Levison HF, Bottke WF, Vokrouhlický D, Gounelle M. COMETARY ORIGIN OF THE ZODIACAL CLOUD AND CARBONACEOUS MICROMETEORITES. IMPLICATIONS FOR HOT DEBRIS DISKS. *ApJ*. 2010 Mar;713(2):816–836. Available from: <https://doi.org/10.1088/0004-637x/713/2/816>.
- Yang H, Ishiguro M. ORIGIN OF INTERPLANETARY DUST THROUGH OPTICAL PROPERTIES OF ZODIACAL LIGHT. *ApJ*. 2015 Oct;813(2):87. Available from: <https://doi.org/10.1088/0004-637x/813/2/87>.
- Rowan-Robinson M, May B. An improved model for the infrared emission from the zodiacal dust cloud: cometary, asteroidal and interstellar dust. *MNRAS*. 2013 01;429(4):2894–2902. Available from: <https://doi.org/10.1093/mnras/sts471>.
- Leinert C, Bowyer S, Haikala LK, Hanner MS, Hauser MG, Levasseur-Regourd AC, et al. The 1997 reference of diffuse night sky

- brightness. *A&AS*. 1998;127(1):1–99. Available from: <https://doi.org/10.1051/aas:1998105>.
11. Lasue J, Levasseur-Regourd AC, Renard JB. Zodiacal light observations and its link with cosmic dust: A review. *Planet Space Sci*. 2020;190:104973. Available from: <https://www.sciencedirect.com/science/article/pii/S0032063319305057>.
  12. Dumont R, Sanchez F. Zodiacal light polarimetry. I. Observations, reductions, disturbing phenomena, accuracy. *A&A*. 1975 Feb;38(3):397–403.
  13. Levasseur-Regourd AC, Dumont R. Absolute photometry of zodiacal light. *A&A*. 1980 Apr;84:277–279.
  14. Murdock TL, Price SD. Infrared measurements of zodiacal light. *AJ*. 1985 Feb;90:375–386.
  15. Matsuura S, Matsumoto T, Matsuura H, Noda M. Rocket-Borne Observations of the Zodiacal Light in the Near-Infrared Wavelengths. *Icarus*. 1995;115(1):199–208. Available from: <https://www.sciencedirect.com/science/article/pii/S0019103585710895>.
  16. Matsumoto T, Kawada M, Murakami H, Noda M, Matsuura S, Tanaka M, et al. IRTS Observation of the Near-Infrared Spectrum of the Zodiacal Light. *PASJ*. 1996 10;48(5):L47–L51. Available from: <https://doi.org/10.1093/pasj/48.5.L47>.
  17. Tsumura K, Matsumoto T, Matsuura S, Pyo J, Sakon I, Wada T. Low-Resolution Spectrum of the Zodiacal Light with the AKARI InfraRed Camera. *PASJ*. 2013 12;65(6):119. Available from: <https://doi.org/10.1093/pasj/65.6.119>.
  18. Buffington A, Bisi MM, Clover JM, Hick PP, Jackson BV, Kuchar TA, et al. Measurements and an empirical model of the Zodiacal brightness as observed by the Solar Mass Ejection Imager (SMEI). *Icarus*. 2016;272:88–101. Available from: <https://www.sciencedirect.com/science/article/pii/S0019103516001238>.
  19. Korngut PM, Kim MG, Arai T, Bangale P, Bock J, Cooray A, et al. Inferred Measurements of the Zodiacal Light Absolute Intensity through Fraunhofer Absorption Line Spectroscopy with CIBER. *ApJ*. 2022 feb;926(2):133. Available from: <https://doi.org/10.3847/1538-4357/ac44ff>.
  20. Takimoto K, Arai T, Matsuura S, Bock JJ, Cooray A, Feder RM, et al. Polarization Spectrum of Near-Infrared Zodiacal Light Observed with CIBER. *ApJ*. 2022 feb;926(1):6. Available from: <https://doi.org/10.3847/1538-4357/ac416f>.
  21. Takimoto K, Matsuura S, Sano K, Feder RM. Near-infrared Polarization Characteristics of the Zodiacal Light Observed with DIRBE/COBE. *ApJ*. 2023 feb;944(2):229. Available from: <https://dx.doi.org/10.3847/1538-4357/acb937>.
  22. Pyo J, Matsumoto T, Jeong WS, Matsuura S. BRIGHTNESS AND FLUCTUATION OF THE MID-INFRARED SKY FROM AKARI OBSERVATIONS TOWARD THE NORTH ECLIPTIC POLE. *ApJ*. 2012 nov;760(2):102. Available from: <https://dx.doi.org/10.1088/0004-637X/760/2/102>.
  23. Kelsall T, Weiland JL, Franz BA, Reach WT, Arendt RG, Dwek E, et al. The COBE Diffuse Infrared Background Experiment Search for the Cosmic Infrared Background. II. Model of the Interplanetary Dust Cloud. *ApJ*. 1998 nov;508(1):44–73. Available from: <https://doi.org/10.1086/306380>.
  24. Wright EL. Angular Power Spectra of the COBE DIRBE Maps. *ApJ*. 1998 mar;496(1):1. Available from: <https://dx.doi.org/10.1086/305345>.
  25. Giese RH, Kneissel B, Rittich U. Three-dimensional models of the zodiacal dust cloud: A comparative study. *Icarus*. 1986;68(3):395–411. Available from: <https://www.sciencedirect.com/science/article/pii/0019103586900461>.
  26. Zook HA, Berg OE. A source for hyperbolic cosmic dust particles. *Planet Space Sci*. 1975;23(1):183–203. Available from: <https://www.sciencedirect.com/science/article/pii/0032063375900781>.
  27. Wehry A, Mann I. Identification of beta -meteoroids from measurements of the dust detector onboard the ULYSSES spacecraft. *A&A*. 1999 Jan;341:296–303.
  28. Krüger H, Grün E. Chapter 29 - Dust in the Solar System. In: Spohn T, Breuer D, Johnson TV, editors. *Encyclopedia of the Solar System* (Third Edition). third edition ed. Boston: Elsevier; 2014. p. 657–682. Available from: <https://www.sciencedirect.com/science/article/pii/B9780124158450000293>.
  29. Szalay JR, Pokorný P, Bale SD, Christian ER, Goetz K, Goodrich K, et al. The Near-Sun Dust Environment: Initial Observations from *Parker Solar Probe*. *ApJS*. 2020 feb;246(2):27. Available from: <https://doi.org/10.3847/1538-4365/ab50c1>.
  30. Leinert C, Grün E. In: Schwenn R, Marsch E, editors. *Interplanetary Dust*. Berlin, Heidelberg: Springer Berlin Heidelberg; 1990. p. 207–275. Available from: [https://doi.org/10.1007/978-3-642-75361-9\\_5](https://doi.org/10.1007/978-3-642-75361-9_5).
  31. Mann I, Kimura H, Biesecker DA, Tsurutani BT, Grün E, McKibben RB, et al. Dust Near The Sun. *Space Sci Rev*. 2004 Jan;110(3):269–305. Available from: <https://doi.org/10.1023/B:SPAC.0000023440.82735.ba>.
  32. Levasseur-Regourd AC, Renard JB, Dumont R. The Zodiacal Cloud Complex. In: Levasseur-Regourd AC, Hasegawa H, editors. *Origin and Evolution of Interplanetary Dust*. Dordrecht: Springer Netherlands; 1991. p. 131–138.
  33. Hanner MS, Sparrow JG, Weinberg JL, Beeson DE. Pioneer 10 observations of zodiacal light brightness near the ecliptic: Changes with heliocentric distance. In: Elsässer H, Fechtig H, editors. *Interplanetary Dust and Zodiacal Light*. Berlin, Heidelberg: Springer Berlin Heidelberg; 1976. p. 29–35.
  34. Leinert C, Richter I, Pitz E, Planck B. The zodiacal light from 1.0 to 0.3 A.U. as observed by the HELIOS space probes. *A&A*. 1981 Nov;103(1):177–188.
  35. Leinert C, Richter I, Pitz E, Hanner M. HELIOS zodiacal light measurements - a tabulated summary. *A&A*. 1982 Jun;110:355–357.
  36. Satoh T, Nakamura M, Ueno M, Uemizu K, Suzuki M, Imamura T, et al. Development and in-flight calibration of IR2: 2- $\mu$ m camera onboard Japan's Venus orbiter, Akatsuki. *Earth, Planets and Space*. 2016 May;68(1):74. Available from: <https://doi.org/10.1186/s40623-016-0451-z>.
  37. Kondo T, Ishihara D, Kaneda H, Nakamichi K, Takaba S, Kobayashi H, et al. MODELING OF THE ZODIACAL EMISSION FOR THE AKARI/IRC MID-INFRARED ALL-SKY DIFFUSE MAPS. *AJ*. 2016 feb;151(3):71. Available from: <https://doi.org/10.3847/0004-6256/151/3/71>.
  38. Hahn JM, Zook HA, Cooper B, Sunkara B. Clementine Observations of the Zodiacal Light and the Dust Content of the Inner Solar System. *Icarus*. 2002;158(2):360–378. Available from: <https://www.sciencedirect.com/science/article/pii/S0019103502968818>.
  39. Stenborg G, Howard RA, Stauffer JR. Characterization of the White-light Brightness of the F-corona between 5° and 24° Elongation. *ApJ*. 2018 aug;862(2):168. Available from: <https://dx.doi.org/10.3847/1538-4357/aacea3>.
  40. Eyles CJ, Harrison RA, Davis CJ, Waltham NR, Shaughnessy BM, Mapson-Menard HCA, et al. The Heliospheric Imagers Onboard the STEREO Mission. *Solar Physics*. 2009 Feb;254(2):387–445. Available from: <https://doi.org/10.1007/s11207-008-9299-0>.
  41. Howard RA, Vourlidis A, Bothmer V, Colaninno RC, DeForest CE, Gallagher B, et al. Near-Sun observations of an F-corona decrease and K-corona fine structure. *Nature*. 2019 Dec;576(7786):232–236. Available from: <https://doi.org/10.1038/s41586-019-1807-x>.
  42. Vourlidis A, Howard RA, Plunkett SP, Korendyke CM, Thernisien AFR, Wang D, et al. The Wide-Field Imager for Solar Probe Plus (WISPR). *Space Science Reviews*. 2016 Dec;204(1):83–130. Available from: <https://doi.org/10.1007/s11214-014-0114-y>.
  43. Grün E, Zook HA, Fechtig H, Giese RH. Collisional balance of the meteoritic complex. *Icarus*. 1985;62(2):244–272. Available from: <https://www.sciencedirect.com/science/article/pii/0019103585901216>.
  44. Divine N. Five populations of interplanetary meteoroids. *Journal of Geophysical Research: Planets*. 1993;98(E9):17029–17048. Available from: <https://agupubs.onlinelibrary.wiley.com/doi/abs/10.1029/93JE01203>.
  45. Poppe AR, Lisse CM, Piquette M, Zemcov M, Horányi M, James D, et al. Constraining the Solar System's Debris Disk with In Situ New Horizons Measurements from the Edgeworth-Kuiper Belt. *ApJL*. 2019 aug;881(1):L12. Available from: <https://dx.doi.org/10.3847/2041-8213/ab322a>.
  46. Bernardoni E, Horányi M, Doner A, Piquette M, Szalay JR, Poppe AR, et al. Student Dust Counter Status Report: The First 50 au. The

- Planetary Science Journal. 2022 mar;3(3):69. Available from: <https://dx.doi.org/10.3847/PSJ/ac5ab7>.
47. Tatsumi E, Kouyama T, Suzuki H, Yamada M, Sakatani N, Kameda S, et al. Updated inflight calibration of Hayabusa2's optical navigation camera (ONC) for scientific observations during the cruise phase. *Icarus*. 2019;325:153–195. Available from: <https://www.sciencedirect.com/science/article/pii/S0019103518304494>.
  48. Riello M, De Angeli, F, Evans, D W, Montegriffo, P, Carrasco, J M, Busso, G, et al. Gaia Early Data Release 3 - Photometric content and validation. *A&A*. 2021;649:A3. Available from: <https://doi.org/10.1051/0004-6361/202039587>.
  49. Cheng AF, Weaver HA, Conard SJ, Morgan MF, Barnouin-Jha O, Boldt JD, et al. Long-Range Reconnaissance Imager on New Horizons. *Space Science Reviews*. 2008 Oct;140(1):189–215. Available from: <https://doi.org/10.1007/s11214-007-9271-6>.
  50. Tsuda Y, Nakazawa S, Yoshikawa M, Saiki T, Terui F, Arakawa M, et al. Chapter 2 - Mission objectives, planning, and achievements of Hayabusa2. In: Hirabayashi M, Tsuda Y, editors. *Hayabusa2 Asteroid Sample Return Mission*. Elsevier; 2022. p. 5–23. Available from: <https://www.sciencedirect.com/science/article/pii/B9780323997317000027>.
  51. Tachibana S, Sawada H, Okazaki R, Takano Y, Sakamoto K, Miura YN, et al. Pebbles and sand on asteroid (162173) Ryugu: In situ observation and particles returned to Earth. *Science*. 2022;375(6584):1011–1016. Available from: <https://www.science.org/doi/abs/10.1126/science.abj8624>.
  52. Mimasu Y, Kikuchi S, Takei Y, Saiki T, ichiro Watanabe S, Tanaka S, et al. Chapter 27 - Extended mission of Hayabusa2. In: Hirabayashi M, Tsuda Y, editors. *Hayabusa2 Asteroid Sample Return Mission*. Elsevier; 2022. p. 557–571. Available from: <https://www.sciencedirect.com/science/article/pii/B9780323997317000027>.
  53. Hirabayashi M, Mimasu Y, Sakatani N, Watanabe S, Tsuda Y, Saiki T, et al. Hayabusa2 extended mission: New voyage to rendezvous with a small asteroid rotating with a short period. *Adv Space Res*. 2021;68(3):1533–1555. Available from: <https://www.sciencedirect.com/science/article/pii/S0273117721002556>.
  54. Kameda S, Suzuki H, Takamatsu T, Cho Y, Yasuda T, Yamada M, et al. Preflight Calibration Test Results for Optical Navigation Camera Telescope (ONC-T) Onboard the Hayabusa2 Spacecraft. *Space Sci Rev*. 2017 Jul;208(1):17–31. Available from: <https://doi.org/10.1007/s11214-015-0227-y>.
  55. Suzuki H, Yamada M, Kouyama T, Tatsumi E, Kameda S, Honda R, et al. Initial inflight calibration for Hayabusa2 optical navigation camera (ONC) for science observations of asteroid Ryugu. *Icarus*. 2018;300:341–359. Available from: <https://www.sciencedirect.com/science/article/pii/S0019103517302257>.
  56. Kouyama T, Tatsumi E, Yokota Y, Yumoto K, Yamada M, Honda R, et al. Post-arrival calibration of Hayabusa2's optical navigation cameras (ONCs): Severe effects from touchdown events. *Icarus*. 2021;360:114353. Available from: <https://www.sciencedirect.com/science/article/pii/S001910352100049X>.
  57. Yamada M, Kouyama T, Yumoto K, Tatsumi E, Takaki N, Yokota Y, et al. Inflight calibration of the optical navigation camera for the extended mission phase of Hayabusa2. *Earth, Planets and Space*. 2023 Mar;75(1):36. Available from: <https://doi.org/10.1186/s40623-023-01789-5>.
  58. Sugita S, Honda R, Morota T, Kameda S, Sawada H, Tatsumi E, et al. The geomorphology, color, and thermal properties of Ryugu: Implications for parent-body processes. *Science*. 2019;364(6437):eaaw0422. Available from: <https://www.science.org/doi/abs/10.1126/science.aaw0422>.
  59. Kameda S, Yokota Y, Kouyama T, Tatsumi E, Ishida M, Morota T, et al. Improved method of hydrous mineral detection by latitudinal distribution of 0.7- $\mu\text{m}$  surface reflectance absorption on the asteroid Ryugu. *Icarus*. 2021;360:114348. Available from: <https://www.sciencedirect.com/science/article/pii/S0019103521000452>.
  60. Lang D, Hogg DW, Mierle K, Blanton M, Roweis S. ASTROMETRY.NET: BLIND ASTROMETRIC CALIBRATION OF ARBITRARY ASTRONOMICAL IMAGES. *AJ*. 2010 mar;139(5):1782–1800. Available from: <https://doi.org/10.1088/0004-6256/139/5/1782>.
  61. Gaia Collaboration, Prusti, T, de Bruijne, J H J, Brown, A G A, Vallenari, A, Babusiaux, C, et al. The Gaia mission. *A&A*. 2016;595:A1. Available from: <https://doi.org/10.1051/0004-6361/201629272>.
  62. Gaia Collaboration, Vallenari A, Brown AGA, Prusti T, de Bruijne JHJ, Arenou F, et al. Gaia Data Release 3. Summary of the content and survey properties. *A&A*. 2022; Available from: <https://doi.org/10.1051/0004-6361/202243940>.
  63. Elvey CT, Roach FE. A Photoelectric Study of the Light from the Night Sky. *ApJ*. 1937 Apr;85:213.
  64. Schlegel DJ, Finkbeiner DP, Davis M. Maps of Dust Infrared Emission for Use in Estimation of Reddening and Cosmic Microwave Background Radiation Foregrounds. *ApJ*. 1998 jun;500(2):525–553. Available from: <https://doi.org/10.1086/305772>.
  65. Sano K, Matsuura S, Tsumura K, Arai T, Shirahata M, Onishi Y. FIRST DETECTION OF GALACTIC LATITUDE DEPENDENCE OF NEAR-INFRARED DIFFUSE GALACTIC LIGHT FROM DIRBE RENALYSIS. *ApJL*. 2016 apr;821(1):L11. Available from: <https://dx.doi.org/10.3847/2041-8205/821/1/L11>.
  66. Jura M. Observational consequences of scattering clouds above the galactic disk. *ApJ*. 1979 Feb;227:798–800.
  67. Arendt RG, Odegard N, Weiland JL, Sodroski TJ, Hauser MG, Dwek E, et al. The COBE Diffuse Infrared Background Experiment Search for the Cosmic Infrared Background. III. Separation of Galactic Emission from the Infrared Sky Brightness. *ApJ*. 1998 nov;508(1):74–105. Available from: <https://doi.org/10.1086/306381>.
  68. Witt AN, Mandel S, Sell PH, Dixon T, Vijn UP. Extended Red Emission in High Galactic Latitude Interstellar Clouds. *ApJ*. 2008 may;679(1):497–511. Available from: <https://doi.org/10.1086/587131>.
  69. Brandt TD, Draine BT. THE SPECTRUM OF THE DIFFUSE GALACTIC LIGHT: THE MILKY WAY IN SCATTERED LIGHT. *ApJ*. 2011 dec;744(2):129. Available from: <https://doi.org/10.1088/0004-637x/744/2/129>.
  70. Ienaka N, Kawara K, Matsuoka Y, Sameshima H, Oyabu S, Tsujimoto T, et al. DIFFUSE GALACTIC LIGHT IN THE FIELD OF THE TRANSLUCENT HIGH GALACTIC LATITUDE CLOUD MBM32. *ApJ*. 2013 mar;767(1):80. Available from: <https://doi.org/10.1088/0004-637x/767/1/80>.
  71. Tsumura K, Matsumoto T, Matsuura S, Sakon I, Tanaka M, Wada T. Low-Resolution Spectrum of the Diffuse Galactic Light and 3.3 $\mu\text{m}$  PAH Emission with the AKARI InfraRed Camera. *PASJ*. 2013 12;65(6):120. Available from: <https://doi.org/10.1093/pasj/65.6.120>.
  72. Arai T, Matsuura S, Bock J, Cooray A, Kim MG, Lanz A, et al. MEASUREMENTS OF THE MEAN DIFFUSE GALACTIC LIGHT SPECTRUM IN THE 0.95-1.65  $\mu\text{m}$  BAND FROM CIBER. *ApJ*. 2015 jun;806(1):69. Available from: <https://doi.org/10.1088/0004-637x/806/1/69>.
  73. Kawara K, Matsuoka Y, Sano K, Brandt TD, Sameshima H, Tsumura K, et al. Ultraviolet to optical diffuse sky emission as seen by the Hubble Space Telescope Faint Object Spectrograph. *PASJ*. 2017 02;69(2):31. Available from: <https://doi.org/10.1093/pasj/psx003>.
  74. Onishi Y, Sano K, Matsuura S, Jeong WS, Pyo J, Kim IJ, et al. MIRIS observation of near-infrared diffuse Galactic light. *PASJ*. 2018 06;70(4):76. Available from: <https://doi.org/10.1093/pasj/psy070>.
  75. Symons T, Zemcov M, Cooray A, Lisse C, Poppe AR. A Measurement of the Cosmic Optical Background and Diffuse Galactic Light Scaling from the  $R < 50$  au New Horizons-LORRI Data. *ApJ*. 2023 mar;945(1):45. Available from: <https://dx.doi.org/10.3847/1538-4357/acaa37>.
  76. Doi Y, Takita S, Ootsubo T, Arimatsu K, Tanaka M, Kitamura Y, et al. The AKARI far-infrared all-sky survey maps. *PASJ*. 2015 06;67(3):50. Available from: <https://doi.org/10.1093/pasj/psv022>.
  77. Takita S, Doi Y, Ootsubo T, Arimatsu K, Ikeda N, Kawada M, et al. Calibration of the AKARI far-infrared all-sky survey maps. *PASJ*.



- 2015 05;67(3):51. Available from: <https://doi.org/10.1093/pasj/psv033>.
78. Yamamura I, Makiuchi S, Koga T, AKARI Team. AKARI Far-Infrared Point Source Catalogues. In: Ootsubo T, Yamamura I, Murata K, Onaka T, editors. *The Cosmic Wheel and the Legacy of the AKARI Archive: From Galaxies and Stars to Planets and Life*; 2018. p. 227–230.
  79. Ootsubo T, Doi Y, Takita S, Nakagawa T, Kawada M, Kitamura Y, et al. AKARI far-infrared maps of the zodiacal dust bands. *PASJ*. 2016 04;68(3):35. Available from: <https://doi.org/10.1093/pasj/psw024>.
  80. Tsumura K, Matsumoto T, Matsuura S, Sakon I, Wada T. Low-Resolution Spectrum of the Extragalactic Background Light with the AKARI InfraRed Camera. *PASJ*. 2013 12;65(6):121. Available from: <https://doi.org/10.1093/pasj/65.6.121>.
  81. Matsumoto T, Kim MG, Pyo J, Tsumura K. REANALYSIS OF THE NEAR-INFRARED EXTRAGALACTIC BACKGROUND LIGHT BASED ON THE *IRTS* OBSERVATIONS. *ApJ*. 2015 jun;807(1):57. Available from: <https://doi.org/10.1088/0004-637x/807/1/57>.
  82. Sano K, Kawara K, Matsuura S, Kataza H, Arai T, Matsuoka Y. Derivation of a Large Isotopic Diffuse Sky Emission Component at 1.25 and 2.2  $\mu\text{m}$  from the COBE/DIRBE Data. *ApJ*. 2015 sep;811(2):77. Available from: <https://doi.org/10.1088/0004-637x/811/2/77>.
  83. Sano K, Kawara K, Matsuura S, Kataza H, Arai T, Matsuoka Y. MEASUREMENTS OF DIFFUSE SKY EMISSION COMPONENTS IN HIGH GALACTIC LATITUDES AT 3.5 AND 4.9  $\mu\text{m}$  USING DIRBE AND *WISE* DATA. *ApJ*. 2016 feb;818(1):72. Available from: <https://doi.org/10.3847/0004-637x/818/1/72>.
  84. Matsuura S, Arai T, Bock JJ, Cooray A, Korngut PM, Kim MG, et al. New Spectral Evidence of an Unaccounted Component of the Near-infrared Extragalactic Background Light from the *CIBER*. *ApJ*. 2017 apr;839(1):7. Available from: <https://doi.org/10.3847/1538-4357/aa6843>.
  85. Mattila K, Väisänen P, Lehtinen K, von Appen-Schnur G, Leinert C. Extragalactic background light: a measurement at 400 nm using dark cloud shadow - II. Spectroscopic separation of the dark cloud's light, and results. *MNRAS*. 2017 05;470(2):2152–2169. Available from: <https://doi.org/10.1093/mnras/stx1296>.
  86. Zemcov M, Immel P, Nguyen C, Cooray A, Lisse CM, Poppe AR. Measurement of the cosmic optical background using the long range reconnaissance imager on New Horizons. *Nature Communications*. 2017 Apr;8(1):15003. Available from: <https://doi.org/10.1038/ncomms15003>.
  87. Lauer TR, Postman M, Spencer JR, Weaver HA, Stern SA, Gladstone GR, et al. Anomalous Flux in the Cosmic Optical Background Detected with New Horizons Observations. *ApJ*. 2022 mar;927(1):L8. Available from: <https://doi.org/10.3847/2041-8213/ac573d>.
  88. Windhorst RA, Carleton R, O'Brien R, Cohen SH, Carter D, Jansen R, et al. SKYSURF: Constraints on Zodiacal Light and Extragalactic Background Light through Panchromatic HST All-sky Surface-brightness Measurements. I. Survey Overview and Methods. *AJ*. 2022 sep;164(4):141. Available from: <https://doi.org/10.3847/1538-3881/ac82af>.
  89. Windhorst RA, Cohen SH, Jansen RA, Summers J, Tompkins S, Conelice CJ, et al. JWST PEARLS. Prime Extragalactic Areas for Reionization and Lensing Science: Project Overview and First Results. *AJ*. 2023 dec;165(1):13. Available from: <https://dx.doi.org/10.3847/1538-3881/aca163>.
  90. Cooray A, Smidt J, De Bernardis F, Gong Y, Stern D, Ashby MLN, et al. Near-infrared background anisotropies from diffuse intrahalo light of galaxies. *Nature*. 2012 Oct;490(7421):514–516. Available from: <https://doi.org/10.1038/nature11474>.
  91. Zemcov M, Smidt J, Arai T, Bock J, Cooray A, Gong Y, et al. On the origin of near-infrared extragalactic background light anisotropy. *Science*. 2014;346(6210):732–735. Available from: <https://www.science.org/doi/abs/10.1126/science.1258168>.
  92. Kashlinsky A. LIGO GRAVITATIONAL WAVE DETECTION, PRIMORDIAL BLACK HOLES, AND THE NEAR-IR COSMIC INFRARED BACKGROUND ANISOTROPIES. *ApJ*. 2016 may;823(2):L25. Available from: <https://doi.org/10.3847/2041-8205/823/2/L25>.
  93. Kohri K, Moroi T, Nakayama K. Can decaying particle explain cosmic infrared background excess? *Physics Letters B*. 2017;772:628–633. Available from: <https://www.sciencedirect.com/science/article/pii/S0370269317305828>.
  94. Matsumoto T, Tsumura K. Fluctuation of the background sky in the Hubble Extremely Deep Field (XDF) and its origin. *PASJ*. 2019 07;71(5):88. Available from: <https://doi.org/10.1093/pasj/psz070>.
  95. Matsumoto T. On the origin of the optical and near-infrared extragalactic background light. *Proc Jpn Acad, Ser B*. 2020 oct;96(8):335–350. Available from: <https://www.ncbi.nlm.nih.gov/pmc/articles/PMC7581960/>.
  96. Zhu W, Wang R. Looking for the signals of the missing baryons in the extragalactic background light. *International Journal of Modern Physics A*. 2023;38(02):2350013. Available from: <https://doi.org/10.1142/S0217751X23500136>.
  97. San M, Herman D, Erikstad, G B, Galloway, M, Watts, D. COSMOGLOBE: Simulating zodiacal emission with ZodiPy. *A&A*. 2022;666:A107. Available from: <https://doi.org/10.1051/0004-6361/202244133>.
  98. Gueymard CA, Myers D, Emery K. Proposed reference irradiance spectra for solar energy systems testing. *Solar Energy*. 2002;73(6):443–467. Available from: <https://www.sciencedirect.com/science/article/pii/S0038092X03000057>.
  99. Matsumoto T, Tsumura K, Matsuoka Y, Pyo J. Zodiacal Light Beyond Earth Orbit Observed with Pioneer 10. *ApJ*. 2018 aug;156(3):86. Available from: <https://doi.org/10.3847/1538-3881/aad0f0>.
  100. Ishiguro M, Yang H, Usui F, Pyo J, Ueno M, Ootsubo T, et al. HIGH-RESOLUTION IMAGING OF THE GEGENSCHIEIN AND THE GEOMETRIC ALBEDO OF INTERPLANETARY DUST. *ApJ*. 2013 mar;767(1):75. Available from: <https://dx.doi.org/10.1088/0004-637x/767/1/75>.
  101. Leinert C, Roser S, Buitrago J. How to maintain the spatial distribution of interplanetary dust. *A&A*. 1983 Feb;118(2):345–357.
  102. Ishimoto H. Modeling the number density distribution of interplanetary dust on the ecliptic plane within 5AU of the Sun. *A&A*. 2000 Oct;362:1158–1173.
  103. van Dijk MHH, Bosma PB, Hovenier JW. Interpretation of the zodiacal light in terms of a finite dust cloud. *A&A*. 1988 Aug;201:373–378.
  104. Giese RH, Kinateder G. The 3-Dimensional Structure of the Interplanetary Dust Cloud. In: Marsden RG, editor. *The Sun and the Heliosphere in Three Dimensions*. Dordrecht: Springer Netherlands; 1986. p. 441–454.
  105. Ishiguro M, Watanabe J, Sarugaku Y, Ootsubo T, Kuroda D, Honda M, et al. 2007 OUTBURST OF 17P/HOLMES: THE ALBEDO AND THE TEMPERATURE OF THE DUST GRAINS. *ApJ*. 2010 apr;714(2):1324. Available from: <https://dx.doi.org/10.1088/0004-637x/714/2/1324>.
  106. Ootsubo T, Onaka T, Yamamura I, Tanabé T, Roellig TL, Chan KW, et al. IRTS observation of the mid-infrared spectrum of the zodiacal emission. *Earth, Planets and Space*. 1998;50(6-7):507–511.
  107. Ootsubo T, Onaka T, Yamamura I, Tanabé T, Roellig TL, Chan KW, et al. IRTS observations of the mid-infrared spectrum of the zodiacal emission. *Adv Space Res*. 2000;25(11):2163–2166. Available from: <https://www.sciencedirect.com/science/article/pii/S0273117799011485>.
  108. Hong SS, Pyo J, Ueno M, Kwon SM, Ishiguro M, Usui F, et al. Modeling of the Interplanetary Dust Cloud. In: Onaka T, White GJ, Nakagawa T, Yamamura I, editors. *AKARI, a Light to Illuminate the Misty Universe*. vol. 418 of ASP Conf. Ser.; 2009. p. 29.
  109. Kuramoto K, Kawakatsu Y, Fujimoto M, Araya A, Barucci MA, Genda H, et al. Martian moons exploration MMX: sample return mission to Phobos elucidating formation processes of habitable planets. *Earth, Planets and Space*. 2022 Jan;74(1):12. Available from: <https://doi.org/10.1186/s40623-021-01545-7>.
  110. Kameda S, Ozaki M, Enya K, Fuse R, Kouyama T, Sakatani N, et al. Design of telescopic nadir imager for geomorphology (TENGOO) and observation of surface reflectance by optical chromatic imager

- (OROCHI) for the Martian Moons Exploration (MMX). *Earth, Planets and Space*. 2021 Dec;73(1):218. Available from: <https://doi.org/10.1186/s40623-021-01462-9>.
111. Matsuura S, Yano H, Yonetoku D, Funase R, Mori O, Shirasawa Y, et al. Joint Planetary and Astronomical Science with the Solar Power Sail Spacecraft. *Transactions of the Japan Society for Aeronautical and Space Sciences, Aerospace Technology Japan*. 2014;12(ists29):Tr\_1–Tr\_5.
  112. Sano K, Matsuura S, Tsumura K, Takahashi A, Hashimoto R, Ogura S, et al. Development of EXo-Zodiacal Infrared Telescope (EXZIT) for observation of visible and near-infrared extragalactic background light. *Proc SPIE*. 2020;11443:114436B. Available from: <https://doi.org/10.1117/12.2559169>.
  113. Ochsenein F, Bauer P, Marcout J. The VizieR database of astronomical catalogues. *A&AS*. 2000;143(1):23–32. Available from: <https://doi.org/10.1051/aas:2000169>.